Nanoscale Advances

ROYAL SOCIETY OF CHEMISTRY

PAPER

View Article Online
View Journal

Cite this: DOI: 10.1039/d0na00912a

Hydrous cobalt–iridium oxide two-dimensional nanoframes: insights into activity and stability of bimetallic acidic oxygen evolution electrocatalysts†

Yuanfang Ying,[a] Jose Fernando Godínez Salomón,[b] Luis Lartundo-Rojas,[c] Ashley Moreno,[b] Robert Meyer,[b] Craig A. Damin[b] and Christopher P. Rhodes *[ab]

Acidic oxygen evolution reaction (OER) electrocatalysts that have high activity, extended durability, and lower costs are needed to further the development and wide-scale adoption of proton-exchange membrane electrolyzers. In this work, we report hydrous cobalt–iridium oxide two-dimensional (2D) nanoframes exhibit higher oxygen evolution activity and similar stability compared with commercial IrO_2; however, the bimetallic Co–Ir catalyst undergoes a significantly different degradation process compared with the monometallic IrO_2 catalyst. The bimetallic Co–Ir 2D nanoframes consist of interconnected Co–Ir alloy domains within an unsupported, carbon-free, porous nanostructure that allows three-dimensional molecular access to the catalytically active surface sites. After electrochemical conditioning within the OER potential range, the predominately bimetallic alloy surface transforms to an oxide/hydroxide surface. Oxygen evolution activities determined using a rotating disk electrode configuration show that the hydrous Co–Ir oxide nanoframes provide 17 times higher OER mass activity and 18 times higher specific activity compared to commercial IrO_2. The higher OER activities of the hydrous Co–Ir nanoframes are attributed to the presence of highly active surface iridium hydroxide groups. The accelerated durability testing of IrO_2 resulted in lowering of the specific activity and partial dissolution of Ir. In contrast, the durability testing of hydrous Co–Ir oxide nanoframes resulted in the combination of a higher Ir dissolution rate, an increase in the relative contribution of surface iridium hydroxide groups and an increase in specific activity. The understanding of the differences in degradation processes between bimetallic and monometallic catalysts furthers our ability to design high activity and stability acidic OER electrocatalysts.

Received 30th October 2020
Accepted 4th February 2021

DOI: 10.1039/d0na00912a

rsc.li/nanoscale-advances

Introduction

Electrolysis of water generates hydrogen that can be used for fuel cells and other applications and be powered by renewable energy sources such as wind and solar power.[1] Water electrolyzers can be coupled with renewable energy sources to store typically unused energy during off-peak times and be used as a load levelling device based on the variable, intermittent nature of wind and solar power generation. Significant challenges for proton exchange membrane water electrolyzers (PEM-WE) include reducing the required input power, reducing the catalyst precious metal content, and improving the catalyst stability.[1–3] In contrast to the fast kinetics for the cathodic hydrogen evolution reaction, the anodic oxygen evolution reaction (OER), which involves the removal of four electrons and protons from water and the formation of an oxygen–oxygen double bond, exhibits sluggish kinetics that results in high overpotentials.[4] For acidic PEM-WEs, platinum-group metals (Ru, Ir, Pt) have been evaluated as acidic OER electrocatalysts.[5–7] Iridium-based catalysts have shown good OER catalytic activities[6] and reasonable stability under the highly corrosive anodic potentials and acidic environment required for OER.[8] Unfortunately, iridium is one of the rarest elements in the Earth's crust with an average mass fraction of 0.001 ppm.[1] To make PEM-WEs feasible on a large scale, the amount of Ir required must be significantly reduced.

To lower the Ir content, improvements in the activity and stability of Ir-based acidic OER catalysts are needed. A number of approaches have been explored including lowering the Ir loading on the electrode,[9] using supported Ir catalysts (*e.g.* TiO_2-

[a]*Materials Science, Engineering and Commercialization Program, Texas State University, San Marcos, TX, 78666, USA. E-mail: cprhodes@txstate.edu*

[b]*Department of Chemistry and Biochemistry, Texas State University, San Marcos, TX, 78666, USA*

[c]*Instituto Politécnico Nacional, Centro de Nanociencias y Micro y Nanotecnologías, UPALM, Zacatenco, CP 07738, Ciudad de México, Mexico*

† Electronic supplementary information (ESI) available: Microscopic, spectroscopic, and electrochemical analysis. See DOI: 10.1039/d0na00912a

supported, SnO_2-supported Ir, *etc.*),[10,11] and increasing the activity of Ir using through substitution with non-precious metals (*e.g.* Ni, Co, Cu, *etc.*).[12–14] Prior density functional theory (DFT) calculations showed that IrO_2 binds adsorbed oxygen too strongly which contributes to increasing the overpotential for the OER.[15] A prior experimental study showed that Ni substituted within IrO_2 resulted in increased OER activity attributed to leaching of Ni atoms, which promote the formation of structurally flexible, reactive OH groups that act as reactive surface intermediates for the OER catalytic reaction.[16] Other work reported that the substitution of Cu within IrO_2 creates oxygen vacancies and changes in the electron occupancy of the t_{2g} and e_g orbital states, resulting in lower overpotentials.[17]

In addition to increasing activity, the stability of OER catalyst remains a significant challenge[1,7,18–20] since all known OER catalysts with reasonable activity (including Ir) dissolve under the highly acidic and oxidative potentials required for oxygen evolution.[7,18,19] Within substituted IrO_2-based catalysts, stability remains a major challenge since many of the metals such as Ni, Co and Cu are thermodynamically unstable in acid at high potentials, as described by Pourbaix diagrams[21] and dissolve under OER testing conditions. Another factor affecting activity and stability is the surface structure. Prior work supports that there are significant surface structure, activity and stability differences between thermally prepared iridium oxides (IrO_2) and amorphous, electrochemically generated iridium oxides (IrO_x).[19] The predominant current understanding of acidic OER catalysts is that activity and stability are inherently linked since they share a common intermediate.[20,22] Prior work on noble metal monometallic oxides established a direct relationship between the high activity and low stability of acidic OER catalysts;[5] however, others' work on RuO_2 catalysts reports no correlation between activity and stability.[23] Recent work suggests that it may be possible to obtain catalysts that are not restricted by the traditional inverse relationship between OER activity and stability.[24]

Cobalt is a potentially promising substituent within IrO_2 for improving OER activity since doping of Co within IrO_2 was shown from DFT calculations to alter the electron density and influence changes in the binding energies of intermediates resulting in structures with lower activation energies.[25] A number of prior studies have evaluated developing improved acidic OER catalysts through interacting iridium and cobalt within iridium–cobalt nanowires,[3] iridium–cobalt porous nanocrystals,[26] iridium–cobalt oxide,[27,28] IrO_2–Co_3O_4 nanorods,[29] and cobalt-doped $SrIrO_3$.[30] Nanoframe structures that combine iridium with Pt[31] or Ni and Cu[32] have been previously studied to enhance the activity and stability of oxygen evolution electrocatalysts. The catalyst structure and resulting OER activity and stability are highly dependent on the starting materials and chemical and electrochemical processes used to generate the active catalyst.[33]

Our group has developed bimetallic two-dimensional (2D) nanoframes that combine highly active bimetallic surface sites and a porous, carbon-free nanoarchitecture to provide oxygen electrocatalysts with improved activity and stability.[14,34,35] The 2D nanoframe structure is synthesized from thermal reduction of precious metal-decorated metal oxide nanosheets and is composed of a unique hierarchical 2D framework containing interconnected solid metallic alloy domains within a porous matrix that provides 3D molecular accessibility. We recently reported unsupported, hydrous iridium–nickel oxide 2D nanoframes exhibit 14 times higher OER mass activity than commercial IrO_2.[14] In this prior study, we used interaction of Ir with Ni within the structure to significantly enhance OER activity and the porous unsupported electrocatalyst structure to provide access to the active sites and avoid support degradation and nanoparticle aggregation. However, the stability of the hydrous iridium–nickel oxide nanoframes was substantially lower than IrO_2. We recently reported the combination of CoIr and NiPt 2D nanoframes function as highly efficient bifunctional oxygen reduction/evolution electrocatalysts;[35] however, our recent study did not explore CoIr nanoframes separately as oxygen evolution catalysts. In this work, we report the morphological and structural characterization of CoIr nanoframes and precursor materials, electrochemical and spectroscopic characterization of the surface structure, and evaluation of the oxygen evolution activity and stability compared with commercial IrO_2 to provide insight into how cobalt interacting with iridium within a 2D nanoframe structure affects OER activity and stability.

Experimental methods

Synthesis

$Co(OH)_2$ nanosheets and iridium-decorated $Co(OH)_2$ nanosheets, notated as $Co(OH)_2$:Ir, were prepared by adapting a microwave-assisted hydrothermal synthesis method previously reported by our group for preparation of $Ni(OH)_2$ and $Ni(OH)_2$:Ir.[14] The synthesis process is summarized in Fig. 1A. The synthesis of Co–Ir nanoframes involved four steps: (i) formation of $Co(OH)_2$ nanosheets using an rapid (10 min) microwave assisted process; (ii) deposition of Ir nanoparticles on α-$Co(OH)_2$ nanosheets; (iii) controlled thermal treatment under reducing atmosphere (H_2/Ar, 5/95 vol%); and (iv) a chemical leaching step in nitric acid (0.05 M HNO_3) to remove unstable metallic Co.

To prepare the $Co(OH)_2$ nanosheets, 1.05 g of $Co(NO_3)_2 \cdot 6H_2O$ (98%, Alfa Aesar) was combined with 0.6486 g of urea (99.3%, Alfa Aesar) in 3 mL of ultrapure water ($\geq$18 MΩ cm, in-house water purification system, Purelab Classic, Evoqua Water Technologies) and 21 mL of ethylene glycol (99%, VWR). The solution was then transferred into a 35 mL microwave vial. The reaction was conducted in a Discover SP Microwave reactor under variable microwave radiation power with a controlled temperature of 120 °C for 10 min under active magnetic stirring. The powder was separated by centrifugation (Sorvall ST16, Thermo) at 3000 RPM for 3 min, rinsed five times with ultrapure water and two times with isopropanol (HPLC grade, VWR), and then dried under ambient atmosphere at 60 °C.

To synthesize iridium-decorated $Co(OH)_2$ nanosheets ($Co(OH)_2$:Ir), 0.038 g of $IrCl_3 \cdot xH_2O$ (99.8%, Alfa Aesar) (equivalent to 20 wt% of Ir *vs.* $Co(OH)_2$) was dissolved in 25 mL of

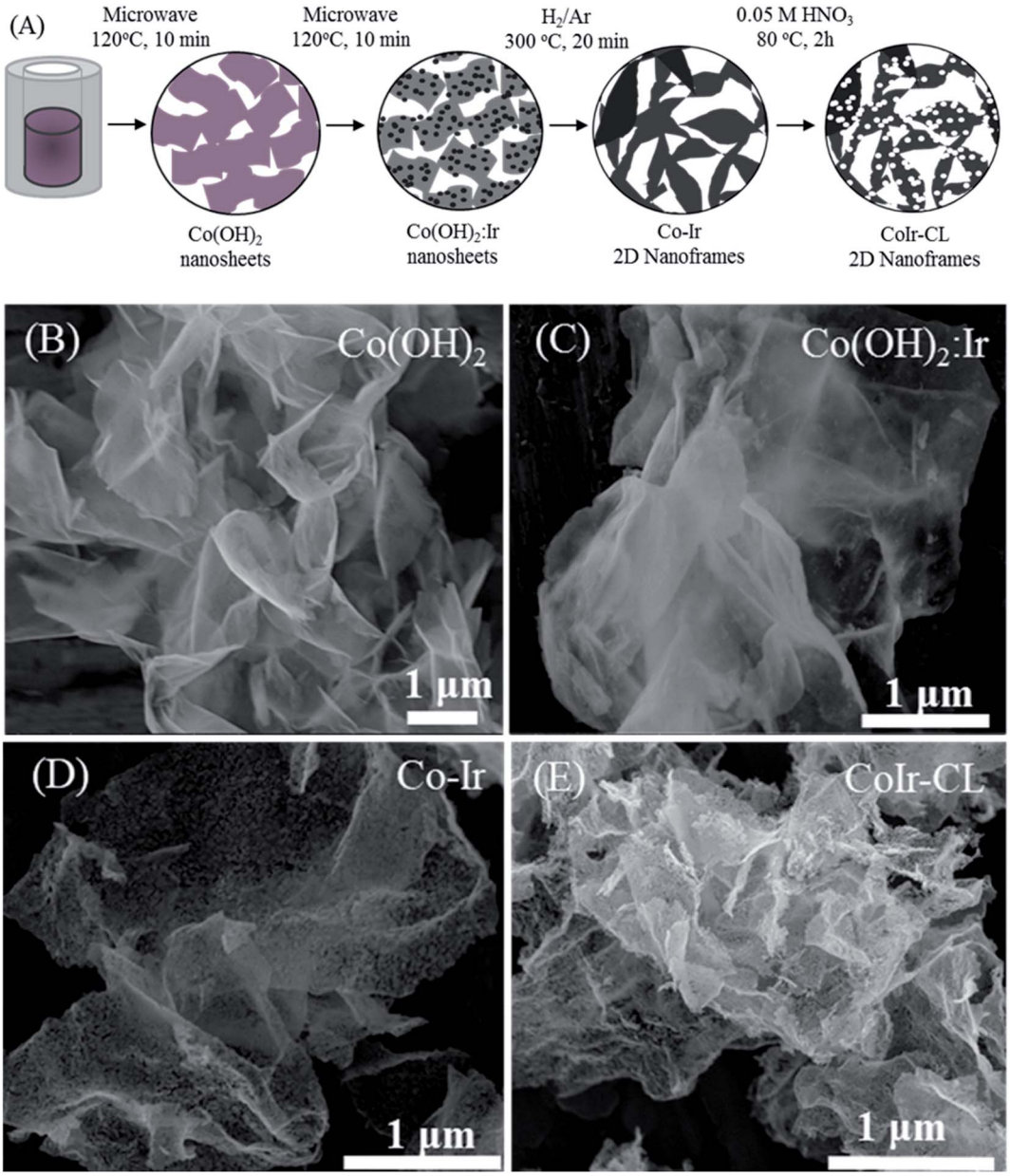

Fig. 1 (A) Schematic representation of the experimental steps for the synthesis of two-dimensional (2D) CoIr-CL nanoframes; representative secondary electron images obtained by scanning electron microscopy (SEM) for (B) $Co(OH)_2$ nanosheets, (C) Ir-decorated $Co(OH)_2$ ($Co(OH)_2$:Ir), (D) after thermal treatment of $Co(OH)_2$:Ir under H_2/Ar at 300 °C (Co–Ir), and (E) after chemical leaching of Co–Ir in 0.05 M HNO_3 at 80 °C for 2 h (CoIr-CL).

ultrapure water, and 0.1 g of $Co(OH)_2$ was added. The suspension was then transferred into a 35 mL microwave vial. The reaction was conducted in a microwave reactor under variable microwave radiation power with a controlled temperature of 120 °C for 10 min with active stirring and then separated using an identical reactor and conditions as described above. The $Co(OH)_2$:Ir nanosheets were thermally treated within a muffle furnace (Lindberg Blue M, Thermo Scientific) at 300 °C for 20 minutes using a ramp rate of 10 °C min^{-1} starting from room temperature and under 120 mL min^{-1} flowing H_2/Ar (5/95 vol%). Then, the reactor was removed from the oven and allowed to cool under H_2/Ar flow until reaching room temperature. The synthesized sample after thermal treatment is notated as Co–Ir. CoIr-CL was prepared by chemically leaching of Co–Ir using a method previously reported by our group.[14,35] Briefly, 0.2 g of the as-prepared Co–Ir nanoframes were dispersed in 100 mL of 0.05 M HNO_3 which was diluted from 70% HNO_3 (99.999%, Aldrich). The solution was bubbled with flowing Ar for 20 min and then heated to 80 °C for 2 hours under stirring. The Ar flow was maintained until the reaction completed. After the reaction, the suspension was cooled to room temperature. The solid was separated by centrifugation at 5000 RPM for 10 min, rinsed five times with ultrapure water, rinsed two times with isopropanol, and then dried at 60 °C. The

samples are noted as $Co(OH)_2$ ($Co(OH)_2$ nanosheets), $Co(OH)_2$:Ir (decorated $Co(OH)_2$ nanosheets with Ir nanoparticles), Co–Ir ($Co(OH)_2$:Ir treated at 300 °C under H_2/Ar), and CoIr-CL (Co–Ir after chemical leaching).

Physical and structural characterization

Scanning electron microscopy (SEM) and energy dispersive X-ray spectroscopy (EDS) elemental mapping were obtained with a Helios NanoLab 400 DualBeam Field Emission Scanning Electron Microscope. The samples were prepared by dispersing the catalyst in isopropanol and coating the sample on an aluminum holder. Powder X-ray diffraction (XRD) measurements were collected using a Bruker AXS D8 Advance powder X-ray diffractometer with a Cu Kα ($\lambda = 1.5406$ Å) radiation source, operating at 40 kV and 25 mA and a high-resolution energy dispersive 1D Linxeye XE detector. The XRD scan range was $5° < 2\theta < 80°$ and used a 0.01° increment.

X-ray photoelectron spectra were obtained using a Thermo Fischer Scientific K-Alpha X-ray photoelectron spectrometer with a monochromatic Al Kα X-ray source, 1486.6 eV, microfocused at the source to give a spot size on the sample of 400 microns in diameter. Samples remained under vacuum for more than 10 h in a prechamber directly connected to the equipment and were then transferred to the analysis chamber with a base pressure of 1×10^{-9} Torr that remained constant during the experiment. Survey and high-resolution spectra were collected using an analyzer, operated in Constant Analyser Energy mode (CAE), with pass energies of 200 and 10 eV, respectively. In order to compensate effects related to charge shift, the $Ir4f_{7/2}$ metal peak at 60.2 eV and the C1s adventitious carbon peak at 284.6 eV were used as internal standards. Data analysis was performed using AVANTAGE v5.91 software (Thermo Fisher Scientific) using a Shirley-type background subtraction and a pseudo-Voigt function with Gaussian (70%)–Lorentzian (30%) for each component. XPS analysis was carried out from two independent batches of each catalyst material to determine any significant changes in the number and content of chemical elements between batches of the same material. In each lot, survey and high-resolution spectra were obtained from three different zones with diameters of 400 microns. From the examination of the survey spectra, it was established that among batches of the same sample the chemical elements present were the same and that these did not present significant changes, ≤1.0, in their atomic percentage content. On the other hand, the high resolution spectra for the Ir5p–Ir4f, O1s and Co2p regions suggested that between batches of the same sample, there were some changes in the atomic percentage content but not in the number of chemical species formed during the synthesis protocol (Fig. S6 and S7†). In view of these results, it was established that both catalytic systems have a homogeneous elemental and chemical species composition. Therefore, for each material average survey and high-resolution spectra from the whole set of data obtained were generated for further analysis. XPS spectra and quantities presented correspond to an average of six measurements from different points of each sample batch.

Attenuated total reflectance Fourier-transform infrared (ATR-FT-IR) spectra of the $Co(OH)_2$ and Co–Ir samples were collected using a Harrick Scientific (Pleasantville, NY) SplitPea ATR microsampling accessory coupled to a Bruker (Billerica, MA) Tensor II FT-IR spectrometer. The SplitPea accessory was equipped with a silicon internal reflection element and utilized a liquid nitrogen cooled mercury–cadmium–telluride detector coupled to the Tensor II spectrometer. The solid samples were brought into direct contact with the silicon internal reflection element using a 0.5 kg loading. Infrared spectra represent the average of 64 individual scans with 4 cm^{-1} resolution. Transmission FT-IR measurements were obtained within the instrument described above using potassium bromide (KBr) pellets prepared by combining the sample with dried KBr powder.

Rotating disk electrochemical characterization

The electrochemical measurements of the catalyst materials were conducted at constant temperature (298 K) in a three-electrode cell using a thin-film rotating disk electrode (TF-RDE) configuration with an Autolab PGSTAT128N bipotentiostat and rotation control (Pine Instruments). A gold disk electrode (RDE, Pine Research instrument, geometric area: 0.196 cm^2) with a thin film of the prepared catalyst was used as the working electrode, and a Pt mesh and a freshly prepared reversible hydrogen electrode (RHE) were used as counter and reference electrodes, respectively.

The electrode fabrication and RDE testing protocols were based on methods previously reported by our group[14,35] and other groups.[36] Catalyst inks were prepared by combining a specific mass (typically ~3 mg) of the acid-leached catalysts (CoIr-CL) with a specific volume of a stock solution to yield a catalyst concentration of 0.43 mg_{cat} mL^{-1}. The stock solution was prepared by mixing 0.4 mL of Nafion suspension (Aldrich, 5 wt%, 1100 g equivalent weight), 20 mL of isopropanol, and 79.6 mL ultrapure water (≥18 MΩ cm). The inks were sonicated (Fisher, 40 kHz) in an ice-bath for 20 minutes. The ink was then immersed in a controlled temperature bath (25 °C) for 1 minute while maintaining agitation and was then used immediately. The inks were applied to a polished Au working electrode (0.196 cm^2 geometric area) and allowed to dry under rotation (700 rpm) under ambient conditions. The electrode loading was controlled by depositing a specific volume of the ink onto the Au working electrode. For the CoIr-CL catalysts, 10 uL was deposited onto the Au electrode which corresponds to a loading of 15.3 μg Ir cm_{geo}^{-2}. After depositing the ink on the rotating Au electrode, the ink was maintained under rotation and allowed to dry under ambient conditions.

The electrochemical characterization of the catalysts was carried out in 0.1 M $HClO_4$ electrolyte prepared with 70% $HClO_4$ (Veritas Doubly Distilled, GFS Chemicals) (0.000001% Cl^-) and ultrapure water. For the electrochemical tests, the Au working electrode was placed in a three-electrode cell with the 0.1 M $HClO_4$ electrolyte. The electrodes were immersed in argon saturated 0.1 M $HClO_4$ under potential control (0.1 V_{RHE}). The catalysts were first conditioned by cycling 20 times from 0.05–1.0 V_{RHE} at 100 mV s^{-1}. The electrochemical surface area (ECSA)

of metallic Ir was calculated by CO-stripping using a specific charge of 358 μC cm^{-2} as the charge corresponding to a monolayer of adsorbed CO.[36] Prior to the analysis in the OER potential range, the catalysts were electrochemically conditioned by cycling between 0.05 to 1.5 V_{RHE} for 60 cycles at a scan rate of 100 mV s^{-1} in argon-saturated 0.1 M $HClO_4$, which is designated as the electrochemical oxidation (EO) step. The electrochemical surface area of IrO_2 ($ECSA_{IrO_2}$) was then determined by measuring the pseudocapacitive charge between 0.3 V and 1.25 V obtained using a scan rate of 50 mV s^{-1} and by subtracting the contribution of the Au disk current collector. The electrochemical surface area was calculated based on the background subtracted pseudocapacitive charge and the coulombic conversion factor of 596 μC $cm_{IrO2}{}^{-2}$.[37]

For evaluating the oxygen evolution reaction activity, the electrode was then conditioned by cycling 10 times in the potential range 1.2–1.8 V_{RHE} at 100 mV s^{-1} and 2500 rpm. Linear sweep voltammetry (LSV) in the potential range of 1.2–1.8 V_{RHE} was performed using a scan rate of 20 mV s^{-1} and a rotation rate of 2500 rpm. Steady-state (iR-corrected) chronoamperometric measurements were then performed by stepping the potential at steps of 0.01 V from 1.3 to 1.6 V_{RHE} while holding for 5 seconds at each potential and rotating the working electrode at 2500 rpm. The internal resistance (iR) values (23–27 Ω) was determined prior to every evaluation using the current interruption method at 1.6 V_{RHE}. The data obtained from chronoamperometric measurements was used for the Tafel plots and for determining the OER mass activity and specific activity. The mass-normalized OER activity was determined by the current at a specific voltage from the chronoamperometric measurements divided by the Ir mass on the electrode. The Ir mass on the electrode was determined by the mass loading and the Ir content within the material determined by inductively coupled plasma mass spectrometry (ICP-MS) analysis for CoIr-CL and for IrO_2 from the certificate of analysis reported by the vendor (84.5 wt%) which was also corroborated by EDS measurements. The actual Ir mass after EO and after accelerated durability testing (ADT) was determined by subtracting the Ir leached into the electrolyte from the initial Ir mass on the electrode. The percent of Ir leached into the solution was determined by ICP-MS after each procedure, EO and ADT, for CoIr-CL and ADT for IrO_2. Inspection of the Tafel plots for linear behavior within specific voltage ranges was used to evaluate that the electrode was not within a mass-transport limited regime within the specific voltage range. Tafel slopes were determined using current obtained from chronoamperometry measurements using the iR-corrected potential between 1.47 V to 1.52 V_{RHE}. After the evaluation of the electrocatalyst in the OER potential range, CV measurements were again obtained to determine the nature of the surface after exposure to OER potentials of up to 1.8 V_{RHE}.

Following the measurements of the OER activity, an accelerated durability test was carried out by maintaining the electrode at a constant potential of 1.6 V_{RHE} for 13.5 hours under a rotation rate of 2500 rpm. After the constant potential step was completed, the electrolyte was replaced, and a 15 minute argon purge was performed to help remove entrapped oxygen bubbles within the catalyst layer which can contribute the influencing the oxygen evolution reaction current using RDE measurements.[38] CV, CO stripping, LSV, and chronoamperometry measurements were then obtained as described above. ICP-MS measurements (PerkinElmer NexIon 2000, Washington University in Saint Louis) were used to analyze the amount of iridium dissolved within the electrolyte after the electrochemical oxidation step and after the accelerated durability test.

Results and discussion

Analysis of the morphology and elemental composition of cobalt–iridium nanoframes and precursor materials

The morphology and elemental composition of the cobalt–iridium nanoframes and precursor materials were determined by scanning electron microscopy (SEM), energy dispersive X-ray spectroscopy (EDS), and inductively coupled plasma atomic emission spectroscopy (ICP-AES). We evaluated the structure at each step of the synthesis process (Fig. 1A) to provide insight into how each step affects the structure of the CoIr-CL catalyst material. The SEM image of the $Co(OH)_2$ nanosheets precursor (Fig. 1B), shows the structure consists of extended ultra-thin nanosheets with lateral sizes in the range of 2–5 μm and thicknesses of ~10 nm. The morphology of the $Co(OH)_2$ nanosheets is similar to that of α-$Ni(OH)_2$ nanosheets synthesized using a similar protocol.[14] After the Ir deposition step, the morphology of $Co(OH)_2$:Ir (Fig. 1C) remained similar to that of the parent $Co(OH)_2$ nanosheet material, but pores were also observed (Fig. S1†). Following thermal treatment of $Co(OH)_2$:Ir under hydrogen, (*i.e.* H_2/Ar, 300 °C), the extended 2D morphology remained; however, significant structural changes occurred, resulting in the formation of Co–Ir 2D nanoframes consisting of interconnected short "nanofilaments" that form a three-dimensional porous network (Fig. 1D). The chemical treatment of Co–Ir in acid maintained the 2D nanoframe morphology (Fig. 1E); in addition, the removal of unstable Co species from Co–Ir resulted in the formation of micropores as detected by scanning transmission electron microscopy measurements, as discussed below.

The changes in the relative elemental composition and distribution of elements within the materials through the synthesis steps were followed by EDS (Fig. 2). In general, the as-prepared, intermediate materials, and final catalyst showed a homogeneous distribution of Co and Ir within the structures. The $Co(OH)_2$:Ir material contained 23.1 ± 3.5 wt% of Ir, very close to the nominal weight ratio determined from weights of the precursors used for the synthesis (*i.e.* 20 wt%), which demonstrates good reaction efficiency. After thermal treatment of $Co(OH)_2$:Ir at 300 °C under H_2/Ar, within Co–Ir the elemental composition of Ir and Co increased to 36.0 ± 1.8 wt% iridium and 46.0 ± 2.9 wt% cobalt and the oxygen content decreased to 17.3 ± 4.3 wt%, which is attributed primarily to the removal of water from the structure as a product of the reaction. After the acid leaching step which selectively removed Co species, the CoIr-CL sample had a content of 88.3 ± 1.5 wt% iridium, 5.2 ± 0.6 wt% cobalt and 6.3 ± 2.0 wt% oxygen. The elemental composition of CoIr-CL determined from EDS was similar to the

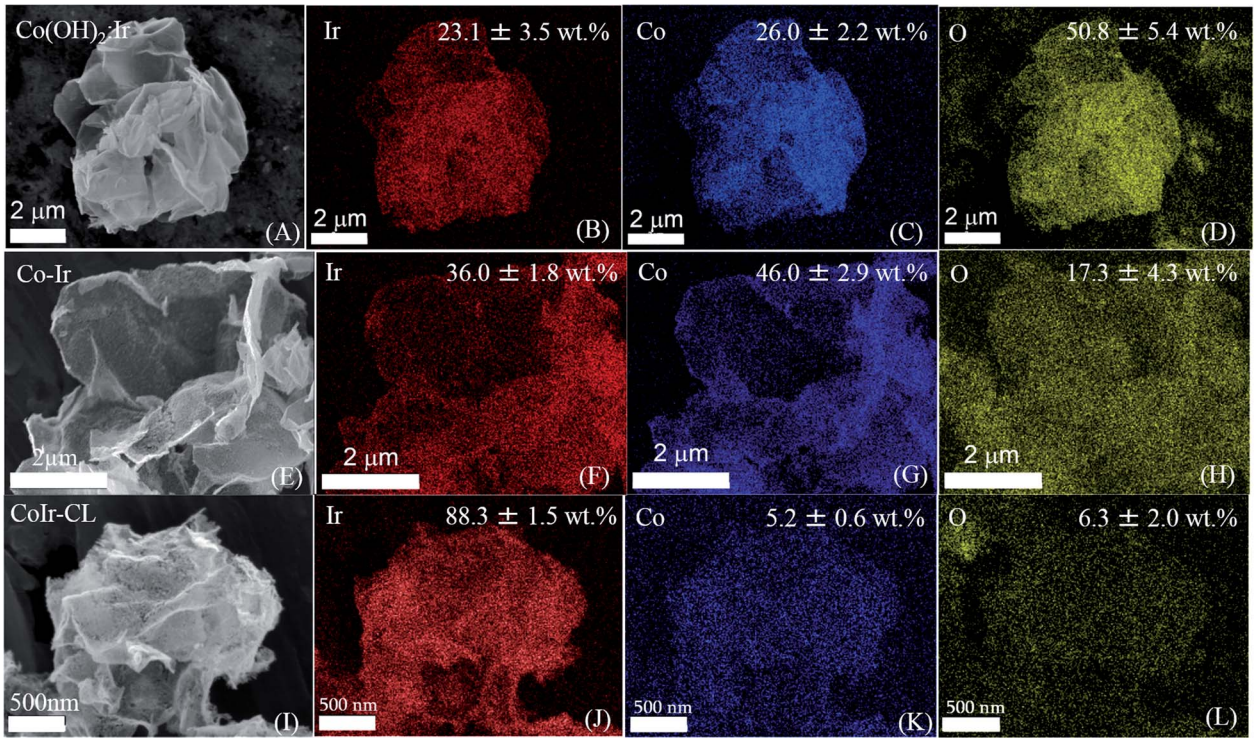

Fig. 2 Scanning electron microscopy (SEM) images and energy-dispersive X-ray spectroscopy (EDS) mapping analysis of $Co(OH)_2$:Ir (A–D); CoIr (E–H); and CoIr-CL (I–L) showing quantification and distribution of iridium, cobalt, and oxygen within the structures.

elemental composition determined by inductively coupled plasma atomic emission spectroscopy (ICP-AES), which yielded a content of 83 ± 2.7 wt% Ir and 9.3 ± 1.0 wt% Co for CoIr-CL. Although metallic Co is thermodynamically unstable in acid,[21] we considered that Co within CoIr-CL could be stabilized from dissolution in acidic electrolyte through interaction of Co with Ir as supported by prior studies of Ni stabilization within IrO_2.[12,14]

X-ray diffraction characterization

The structures of the precursor materials and final catalyst were determined using powder X-ray diffraction (XRD). Shown in Fig. 3 are the powder XRD patterns for $Co(OH)_2$, $Co(OH)_2$:Ir, Co–Ir, and CoIr-CL along with patterns obtained from the crystallography open database (COD) used as references: α-$Co(OH)_2$ (96-900-9102), Co_3O_4 (96-900-5893), metallic Co (96-901-0969) and metallic Ir (96-901-2961). The XRD pattern of $Co(OH)_2$ exhibited a strong reflection at a 2θ value of 12.1°, assigned to the (001) basal plane arising from the preferential orientation of the nanosheets.[39] The slight differences of the diffraction angles of the synthesized α-$Co(OH)_2$ compared with a prior study[39] may be related with changes of the interlayer spacing and structural disorder, produced by the presence of different intercalated anions and/or differences in water content.[34,39–41] The presence of water and ethylene glycol (EG) species within the synthesized α-$Co(OH)_2$ was further confirmed by Fourier-transform infrared spectroscopy as discussed below. We note that the presence of ethylene glycol and water within α-$Co(OH)_2$ may play an important role in the formation of the nanosheet structure.

After Ir deposition, the XRD pattern of $Co(OH)_2$:Ir showed the strong peak associated with the (001) basal plane of $Co(OH)_2$ disappeared, while small peaks around 18° and 59° associated with a Co_3O_4 phase were present. The disappearance of the (001) peak within $Co(OH)_2$:Ir is attributed to the disruption of the basal plane which may be influenced by the creation of pores within the structure as observed by microscopy (Fig. S1†).

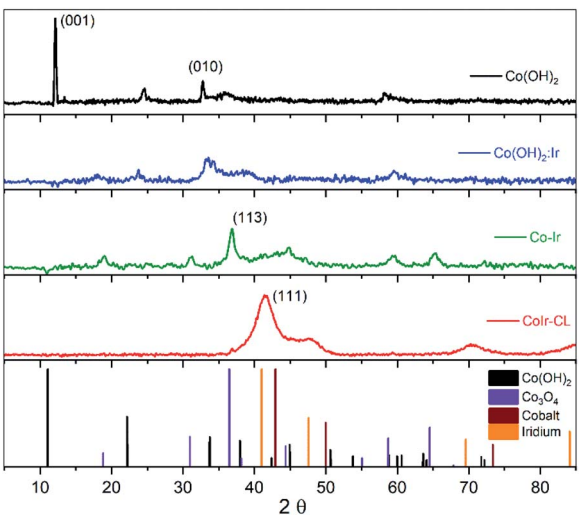

Fig. 3 Powder X-ray diffraction (XRD) patterns of $Co(OH)_2$, $Co(OH)_2$:Ir, Co–Ir, CoIr-CL and patterns for references (α-$Co(OH)_2$, Co_3O_4, Co, and Ir).

The deposition of Ir onto the $Co(OH)_2$ nanosheets may result in the displacement of oxygen by Ir species due to galvanic displacement which modifies the oxygen stoichiometry due to oxygen depletion[28] or may occur *via* ethylene glycol reduction.[42,43]

After thermal treatment of $Co(OH)_2$:Ir under hydrogen, the XRD patterns of Co–Ir showed significant morphological and structural changes. The XRD pattern of Co–Ir showed the presence of peaks consistent with Co_3O_4 (at ~18°, 32°, 37° and 65°).[39] The presence of Co_3O_4 within Co–Ir was also supported by infrared spectroscopic analysis (described below). The XRD pattern of Co–Ir showed wide peaks between 40° to 50° which may be associated with low intensity (111) reflections of small crystalline domains and/or microstrain from a metallic face-centered cubic CoIr structure.[44,45] The presence of a poorly crystalline metallic Co–Ir phase is supported by the magnetic response of Co–Ir to a lab magnet; however, further work is needed to confirm the metallic character. We note that the XRD pattern of Co–Ir prepared by thermal treatment at 300 °C in H_2/Ar was significantly different than the XRD previously reported of NiIr treated under identical conditions.[14] In the case of NiIr, we observed the presence of peaks that correspond to a metallic NiIr phase and no NiO peaks; in contrast, for CoIr, we did not observe defined peaks corresponding to metallic CoIr phase and did observe peaks consistent with Co_3O_4. The differences in the thermal reduction of $Ni(OH)_2$:Ir and $Co(OH)_2$:Ir to NiIr and CoIr respectively suggests that oxygen binding to Co may be stronger than oxygen binding to Ni within the structure.

After the acidic treatment of Co–Ir, most of the Co species that were not stabilized within the Ir structure were removed as shown from EDS analysis (Fig. 2). The XRD pattern of CoIr-CL shows peaks at 41.2° and 46.9° that are associated with the (111) planes (2θ = 40.6°) and (200) planes (2θ = 47.3°) of metallic Ir. The peak position of the Ir(111) reflection is shifted to higher 2θ values compared to the characteristic position of a metallic Ir lattice. A lattice constant of 3.771 Å was calculated from the peak position of the (111) plane using a face-centered cubic cell. The lattice constant of 3.771 Å for the CoIr-CL material is smaller than the standard metallic iridium lattice constant of 3.831 Å, indicating a ~1.6% lattice contraction. These observations support a lattice disruption of iridium likely due to the inclusion of residual Co within the Ir structure in agreement with STEM data, as presented below. In addition, very low intensity peaks around 36° and 60° assigned to trace Co_3O_4 within the structure are still observed.

Fourier-transform infrared spectroscopy analysis

Attenuated total reflectance Fourier-transform infrared spectroscopy (ATR-FT-IR) measurements were performed to characterize the $Co(OH)_2$, Co–Ir, CoIr-300, and CoIr-CL materials, and ATR-FT-IR spectra are shown in Fig. 4. The ATR-FT-IR spectrum of the as-prepared $Co(OH)_2$ nanosheets, Fig. 4a, shows absorptions at 3500 and 1632 cm^{-1} that are respectively assigned to the O–H stretching and H–O–H bending vibrations of water within the interlayer region.[46–57] The absorption at 3617 cm^{-1} is consistent with a non-hydrogen bonded O–H

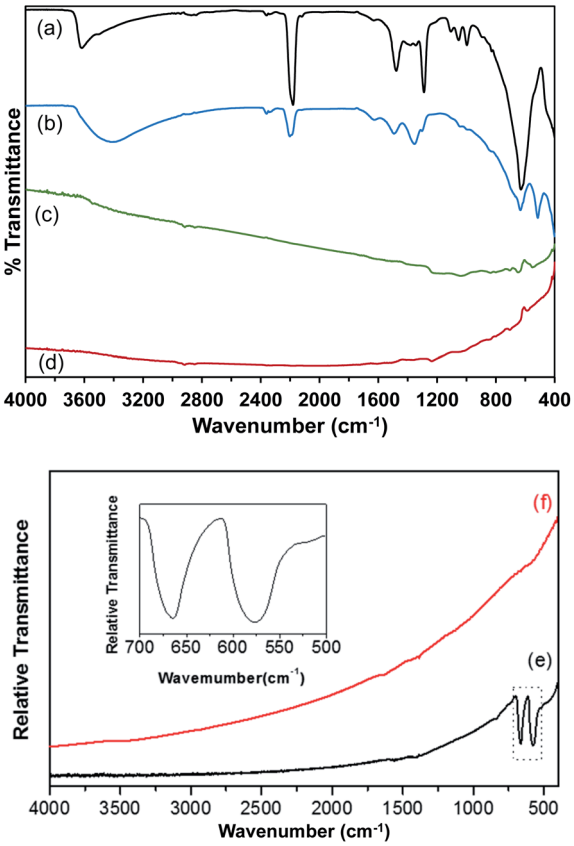

Fig. 4 Attenuated Total Reflectance Fourier-Transform Infrared spectra (ATR-FT-IR) of (a) $Co(OH)_2$; (b) $Co(OH)_2$:Ir; (c) Co–Ir; and (d) CoIr-CL; transmission Fourier-transform infrared spectra (FT-IR) of (e) Co–Ir; and (f) CoIr-CL obtained using KBr pellets; inset shows a magnification of the absorption bands at 670 cm^{-1} and at 578 cm^{-1} of Co–Ir.

stretch in $Co(OH)_2$.[53,56,58,59] The 630 cm^{-1} absorption is characteristic of the Co–O–H bending mode.[53,55,56] Absorptions over the range of 2980–2839 cm^{-1} are assigned to C–H stretches, potentially resulting from residual ethylene glycol intercalated between the $Co(OH)_2$ nanosheets. A previous study discussed ethylene glycol molecules capping the outside of α-$NiOH_2$ nanosheets.[60] The 1289 cm^{-1} absorption could correspond to either the OH deformation of a 1° alcohol, such as ethylene glycol, or a symmetric nitrate stretch. The 1106 cm^{-1} absorption could result from either the C–O–CN stretch of a cyanate or the C–O stretch of a 2° alcohol. Residual isopropanol, which was used to rinse the solid $Co(OH)_2$ following centrifugation, could remain in the solid following drying. The asymmetric stretch of a cyanate (OCN^-), a byproduct of urea hydrolysis, is assigned to the 2180 cm^{-1} absorption.[47,49,51,52,54,57,61–63] Soler-Illia *et al.* proposed that, in addition to CO_3^{2-}, OCN^- anions replaced lattice OH^- anions in α-$Ni(OH)_2$.[47] The 1053 cm^{-1} absorption could be related to either a free nitrate stretching mode[6,64,65] or the C–O stretch of ethylene glycol.[66] Peaks at 1105, 1054, and 998 cm^{-1} are attributed to the ν(C–O) modes of ethylene glycol[66] and ν_1 mode of nitrate.[48,53]

A prior study of α-hydroxides, including those of cobalt and nickel, supports that the materials generally contain a significant amount of intercalated anions.[61] Within the ATR-FT-IR spectrum of $Co(OH)_2$ nanosheets, Fig. 4a, surface and intercalated nitrates were assigned to the absorptions at 1381, 1345, 997, and 829 cm^{-1}.[50,52,56,57,60,63,64] The nitrate absorptions at 1381, 1345, and 829 cm^{-1} correspond to free NO_3^- ions with D_{3h} point group symmetry.[48,53,67] Upon coordination to a metal, the local symmetry of the NO_3^- is lowered to a C_{2v} symmetry.[68,69] The remaining nitrate absorption at 997 cm^{-1} is assigned to coordinated NO_3^- ions in the $Co(OH)_2$ structure with C_{2v} symmetry.[65] The presence of nitrate absorptions in the ATR-FT-IR spectra of the as-prepared $Co(OH)_2$ nanosheets suggests that NO_3^- from $Co(NO_3)_2 \cdot 6H_2O$ is carried through the synthesis procedure and exists in two different environments within the material.[64] The ν_1 mode of NO_3^- is usually IR-inactive; however, the presence of intercalated water between the $Co(OH)_2$ nanosheets could result in a NO_3^- environment in which the ν_1 mode of NO_3^- becomes weakly IR-active.[64] The presence of free CO_3^{2-} ions with D_{3h} point group symmetry is indicated by absorptions at 1478 and 889 cm^{-1}.[50,52,68] The presence of carbonate within the sample could result from the dissolution of CO_2 in the aqueous solutions prior to urea hydrolysis. In addition, carbonate anions could be generated by the decomposition of urea, as previously proposed.[47]

The ATR-FT-IR spectrum of $Co(OH)_2$:Ir is shown in Fig. 4b. Following iridium deposition onto the $Co(OH)_2$ nanosheets, changes to the $Co(OH)_2$ spectrum are observed. The δ(Co–O–H) peak is shifted to 632 cm^{-1} while a new peak with greater relative intensity appears at 510 cm^{-1} in the $Co(OH)_2$:Ir spectrum. Bands for carbonate and nitrate ν_3 modes were blue shifted to 1495 and 1365 cm^{-1} respectively. Absorptions at 3417 and 1627 cm^{-1} indicate the presence of surface or interlayer water. The Co–O–H deformation and Co–O stretch of $Co(OH)_2$ are assigned to the absorptions at 633 and 401 cm^{-1}, respectively. The absorption at 515 cm^{-1} is in the range of bands observed for ν(Ir–O)[70] and ν(Co–O)[71] modes; and further analysis is needed to determine the specific assignment of this band within $Co(OH)_2$:Ir.

The remaining absorptions in the $Co(OH)_2$:Ir spectrum are associated with surface and interlayer species that are present in the as-prepared $Co(OH)_2$ precursor. The 2201 cm^{-1} absorption is attributed to the asymmetric OCN^- stretch. The presence of free NO_3^- ions was determined based on the 1354 and 828 cm^{-1} absorptions. The absorption at 1493 cm^{-1} is assigned to the ν_3 mode of CO_3^{2-}.[52] The O–H deformation and C–O stretching modes at 1303 and 1040 cm^{-1}, respectively,[66] support the presence of residual ethylene glycol within $Co(OH)_2$:Ir. The nitrogen species band is blue shifted to 2200 cm^{-1} and is greatly reduced in intensity following iridium deposition. Broadening and red shifting of the ν(O–H) band, as well as increased relative intensity of the δ(H_2O) band, suggest incorporation of more water molecules into the structure during the deposition process. Broadening and shifting of the ν(O–H) bands is consistent with increased hydrogen bonding within the structure.[54] The reduction in the relative intensity of bands arising from ethylene glycol between the spectrum of $Co(OH)_2$ and $Co(OH)_2$:Ir suggests that it is possible that ethylene glycol may act as a reducing agent to reduce Ir^{3+} to Ir during the deposition process as supported by prior work on formation of colloidal Ir and other platinum-group metal nanoparticles,[42,43] or alternatively ethylene glycol is removed during the Ir deposition process; however, further analysis is needed to determine the potential role of ethylene glycol during the deposition process.

Fig. 4c shows the ATR-FT-IR spectrum of a Co–Ir sample following a thermal treatment at 300 °C of $Co(OH)_2$:Ir for 20 minutes. The ATR spectrum of the resulting black solid indicated that the sample strongly absorbed the infrared radiation and possessed a highly metallic character. Dehydration of the sample was apparent by the lack of water related absorptions. The effect of scattering of the infrared radiation by the Co–Ir sample is apparent by the sloping baseline. For strongly absorbing samples, light scattering within the sample causes the baseline to slope upwards with increasing wavenumbers.[72] The ATR spectrum of the CoIr-CL sample following chemical leaching of the cobalt, Fig. 4d, also indicated the presence of a highly metallic phase.[70]

Since the ATR spectra of Co–Ir and CoIr-CL did not show clearly resolved bands relative to the baseline consistent with their metallic character as described above, transmission FT-IR measurements of samples within potassium bromide (KBr) pellets were made. Shown in Fig. 4e and (f) are the transmission FT-IR spectra of Co–Ir and CoIr-CL, respectively. The FT-IR spectrum of Co–Ir (Fig. 4e) has only two defined peaks at 670 and 578 cm^{-1} whose wavenumbers are generally consistent with the positions of bands from Co_3O_4 modes based on a prior study that reported two distinct and sharp bands at 568 (ν_1) and 664 (ν_2) cm^{-1} which originate from the stretching vibrations of the Co–O bonds within spinel Co_3O_4.[71] The ν_1 band is characteristic of a Co^{3+}–O vibration in an octahedral site, and the ν_2 band is attributed to a Co^{2+}–O vibration in a tetrahedral site in the spinel lattice.[73] Our X-ray diffraction data showed the presence of peaks consistent with Co_3O_4. It is also possible that the 578 cm^{-1} band originated from a Ir–O stretching mode based on a prior study;[70] however, our X-ray diffraction data did not show the presence of any IrO_x phase.

Scanning transmission electron microscopy characterization

High-angular dark-field scanning transmission electron microscopy (HAADF-STEM) images of CoIr-CL after chemical leaching were obtained to evaluate the atomic-level structure (Fig. 5). The low magnification STEM image (Fig. 5A) confirmed the existence of extended 2D framework created by the highly porous network of interconnected short nanofilaments. From nitrogen physisorption analysis, our group reported that the majority of pores within CoIr-CL nanoframes are within the 2–50 nm (mesopore) and >50 nm (macropore) range.[35] The porous network within CoIr-CL may play an important role in mass transport processes since in particular mesopores (2–50 nm) within the structure facilitate reactant/product mass transport to the active catalyst sites.[37,74]

The high-resolution HAADF-STEM image (Fig. 5B) and fast Fourier transform (FFT) pattern (Fig. 5D) demonstrate the

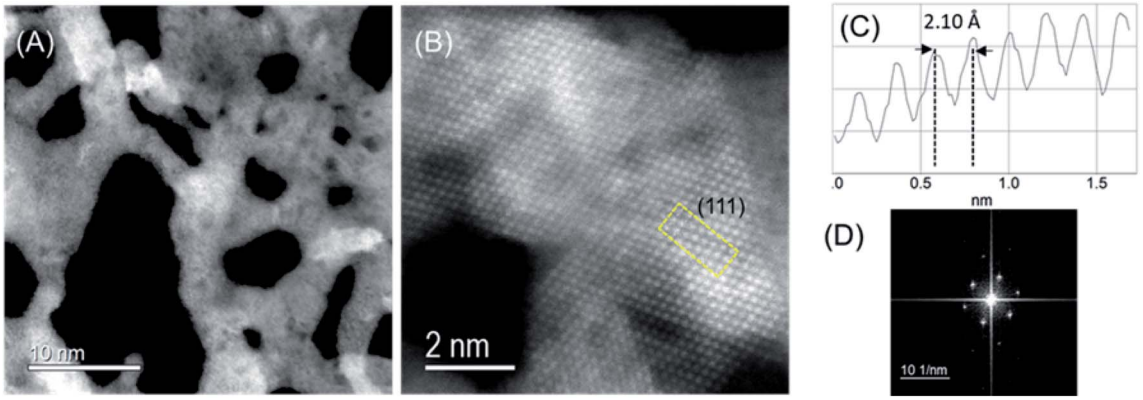

Fig. 5 Low-magnification (A) and high resolution (B) high-angular dark-field scanning transmission electron microscopy (HAADF-STEM) images of CoIr-CL catalyst. The yellow box in (B) indicates the area used for the HAADF-STEM intensity profile shown in (C) which shows an interplanar distance consistent with (111) lattice plane; (D) fast Fourier transform (FFT) of the boxed area in yellow in (B).

single-crystalline nature of domains within the material. The intensity profile (Fig. 4C) shows an average lattice spacing of 0.213 ± 0.009 nm corresponding to the (111) lattice plane of bimetallic CoIr-CL, according to a face-centered cubic (fcc) structure identified by XRD (Fig. 3), and confirmed a lattice compression with respect to the metallic iridium pattern taken as the standard (0.216 nm).[35] The HAADF-STEM and corresponding EDS mapping images of CoIr-CL (Fig. S2†) show uniformly dispersed Co and Ir, consistent with the XRD data. The elemental composition of Ir, Co, and O from HAADF-STEM EDS is in a similar range as values obtained from SEM EDS analysis (Fig. 2).

Characterization of the surface region using X-ray photoelectron spectroscopy

X-ray photoelectron spectroscopy (XPS) was used to identify and perform semi-quantitative analysis of chemical species within the surface region of the catalyst materials. A comparison of the average survey spectra acquired from the surfaces of commercial IrO_2 and CoIr-CL is shown in Fig. S3.† For both samples, iridium, chlorine, carbon, nitrogen, oxygen and sodium core-level peaks were clearly observed and identified (sodium peak not shown). In addition to iridium, cobalt, and oxygen, the presence of carbon, chlorine, nitrogen, and sodium within the samples was observed and is attributed to the precursors used during the synthesis process. As expected, the cobalt core-level peak was only observed in the CoIr-CL material.

Semi-quantitative analysis of the XPS average survey spectra was used to estimate the atomic composition within the surface region (Table 1). Analysis of the survey spectra of CoIr-CL and IrO_2 supports that a higher degree of oxygen is present within the surface region of IrO_2 (52.3 atomic% oxygen) compared to CoIr-CL (33.3 atomic% oxygen). The weight percentages of Ir, Co and O within the surface region determined from XPS are in general agreement with values obtained from SEM-EDS analysis (Fig. 2I–L); however, XPS analysis showed a slightly lower surface concentration of Ir and a slightly higher concentration of O and Co species compared to SEM-EDS analysis (Table S1†) which may be due to differences in probing of the surface region between these methods.

Spectral fitting of Ir5p–Ir4f region. High resolution XPS spectra of CoIr-CL and IrO_2 samples within the Ir5p–Ir4f region were collected, and peak fitting was utilized to identify and estimate the relative atomic percentage of iridium surface chemical species. The XPS spectra and fitted peaks within the Ir4f region for CoIr-CL and IrO_2 are shown in Fig. 6A. Details of the peak fitting analysis of the Ir5p–Ir4f peak binding energies, relative areas, and assignments are provided in Table 2. Additional details of the basis for specific peak assignments, fitting of the Ir5p region, and fitting of the Co3p peaks within the Ir4f region are included in Table S2, Fig. S4 and ESI.† The XPS fitting analysis of the Ir4f region supports that the surface region of CoIr-CL and commercial IrO_2 contain anhydrous IrO_2 (labelled Ir_1), hydrous IrO_2 (labelled Ir_3), and either Ir_2O_3 or an iridium chloride species (labelled Ir_2). In the case of CoIr-CL, two additional peaks were needed to perform Ir5p–Ir4f high resolution spectra fitting: a peak corresponding to the Co3p region, labelled Co3p, and a peak corresponding to metallic iridium, labelled Ir^0, as shown in Fig. 6A. The relative surface content of anhydrous IrO_2, hydrous IrO_2, and either Ir_2O_3 or an iridium chloride species was lower within CoIr-CL compared to commercial IrO_2; however, the CoIr-CL sample

Table 1 Relative weight and atomic percentages of iridium, cobalt, oxygen and elements related to precursors within the surface region of the commercial IrO_2 (Alfa) and CoIr-CL determined from analysis of survey X-ray photoelectron spectra

		Element						
Sample	Content[a]	Ir	Co	O	C	N	Cl	Na
IrO_2	Weight%	75.0	—	17.5	6.8	0.4	0.3	
	Atomic%	18.7	—	52.3	27.2	1.4	0.4	
CoIr-CL	Weight%	75.0	6.7	9.6	7.4	0.9	0.2	0.2
	Atomic%	21.7	6.4	33.3	34.3	3.4	0.4	0.5

[a] Average content from six spectra.

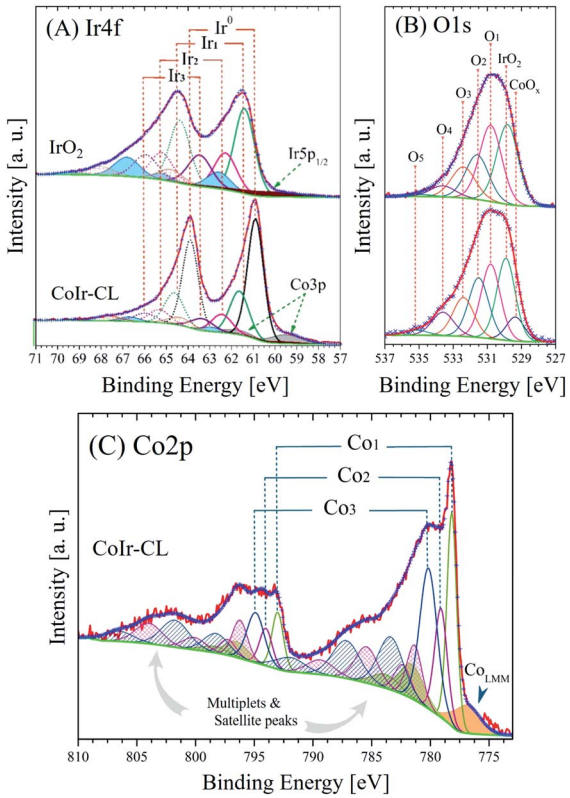

Fig. 6 High-resolution X-ray photoelectron spectra and fitted peaks of (A) Ir4f and (B) O1s regions of commercial IrO_2 and CoIr-CL samples and (C) Co2p region of CoIr-CL; the intensities of Ir4f and O1s core level spectra were normalized; details of peak fitting analysis and label are discussed in the text and in Table 2.

also contained metallic Ir (labelled Ir^0) within the surface region.

Spectral fitting of O1s region. The surface oxygen species are of importance to the oxygen evolution reaction, particularly since prior studies have shown OER reaction mechanisms can involve the participation of lattice oxygen.[75] High resolution XPS spectra of CoIr-CL and IrO_2 samples within the O1s region and fitted peaks are shown in Fig. 6B. Details of the O1s fitted peaks and the basis for peak assignments is provided in Tables 2 and S3 and ESI.† The fitting analysis identified five different surface oxygen species and an additional peak in the case of the CoIr-CL sample, labelled CoO_x, which was assigned to Co_3O_4. We note that the presence of some Co_3O_4 within CoIr-CL was also supported by XRD data (Fig. 3). The peak with a binding energy of 529.6 eV was assigned to oxygen within an anhydrous IrO_2 structure (labelled "IrO_2"). The peak labelled O_1 is attributed to an iridium sub-oxide (Ir_2O_3) and/or carbonate species. The peak labelled O_2 is related iridium hydroxides and oxyhydroxides ($Ir(OH)_3$ or IrOOH). The peaks labeled O_3, O_4 and O_5 are attributed to species from precursors and adsorbed species, as described in Table 2. The comparison of the O1s region of CoIr-CL and commercial IrO_2 supports that the relative surface concentration of O_2 and O_3 species is higher within CoIr-CL compared with commercial IrO_2 and the CoIr-CL sample contains Co_3O_4 within the surface region.

Spectral fitting of Co2p region. The high resolution XPS spectra of CoIr-CL within the Co2p region and fitted peaks are shown in Fig. 5C, and peak assignments are provided in Table 2. Details of the fitting analysis of the complex Co2p region which involves multiple surface species, multiplet splitting and satellite bands is presented in Fig. S6, S7, Table S4 and ESI.† Based on the fitting analysis, the surface of the CoIr-CL catalyst contained metallic Co, labelled as Co_1, and cobalt within both Co^{2+} and Co^{3+} oxidation states assigned to Co_3O_4 (labelled as Co_2) and CoO, Co(OH) and/or CoOOH (labelled as Co_3). The presence of metallic cobalt is supported by the high relative intensity peak located around 778.2 ± 0.2 eV which is good agreement with SAED pattern obtained by STEM and XRD data, discussed above. Regarding the peak labelled Co_2, associated with Co_3O_4, even though its BE was particularly low, 779.1 ± 0.2 eV, with respect to those generally reported,[2,76–81] the presence of Co_3O_4 within CoIr-CL is supported by the existence of its satellite structures, Table 2, as well as XRD data (Fig. 3). Based on the fitting results of Co2p and O1s regions, the Co_3 contribution was considered to mainly consist of $Co(OH)_2$, CoOOH, and/or CoO.

Surface characterization using cyclic voltammetry and carbon monoxide stripping voltammetry

The CoIr-CL and IrO_2 catalysts were electrochemically analyzed using a thin-film rotating disk electrode technique.[82] Cyclic voltammetry (CV) of CoIr-CL was used to characterize the initial catalyst surface and the evolution of the surface following an electrochemical oxidation protocol (Fig. 7). After initial conditioning by cycling at low potential range ($E \leq 1.0$ V_{RHE}) in O_2-free 0.1 M $HClO_4$, the CoIr-CL catalyst (Fig. 7A, black curve) exhibited distinctive hydrogen adsorption/desorption features associated with hydrogen underpotential deposition (H_{upd}) on a metallic Ir surface.[83] No peak associated with the oxidation of the non-noble species (*i.e.* Co) was observed during the first cycle,[84] corroborating the formation of a stable metallic Ir-rich surface after the chemical leaching step. The presence of metallic surface features is consistent with the metallic phase observed from STEM and XPS measurements (Fig. 5 and 6A). In addition, oxidation/reduction peaks due to reversible IrO_x formation/reduction at $E \geq 0.5$ V_{RHE} were also observed.[83] Carbon monoxide (CO) stripping voltammetry measurements (Fig. 7B) also support the presence of a metallic Ir-rich surface on the CoIr-CL material. From the integration of the CO stripping peak, the calculated electrochemical surface area of Ir ($ECSA_{Ir,CO}$) was 61.2 ± 3.1 m^2 g^{-1} which is comparable with the BET surface area of CoIr-CL of 57 ± 7 m^2 g^{-1} previously reported by our group,[35] supporting a high dispersion of Ir on the surface. In addition, the electrochemical surface area of CoIr-CL is reasonably high compared to the electrochemical surface area of commercial IrO_2 (Alfa Aesar) of 25.3–28.7 m^2 g^{-1} determined by pseudocapacitance and mercury underpotential deposition measurements.[14,85]

Similar to as observed within our prior work on NiIr nanoframes,[14] the CoIr-CL catalyst showed that the predominantly metallic nature of the surface of the electrocatalyst was altered

Table 2 Details of peak fitting analysis of X-ray photoelectron spectra of Ir5p–Ir4f regions of CoIr-CL and IrO_2; O1s regions of CoIr-CL and IrO_2; and Co2p regions of CoIr-CL including binding energy (BE), full width at half maximum (FHWM), and relative areas, labels, and assignments; details supporting assignments are provided in ESI

Region	Sample	BE [±0.1 eV]	FWHM [eV]	Area[a] [at%]	Label	Assignment
Ir4f	IrO_2	≈60.8	4.2	43.2	$Ir5p_{1/2}$	Metal, oxide and hydroxide range
		61.4	1.1	29.8	Ir_1	IrO_2
		62.3	1.2	14.2	Ir_2	Ir_2O_3, $IrCl_3 \cdot xH_2O$, $IrCl_x$ and/or $IrCl_3$
		62.6	1.2	—	—	Ir(IV) Sat I
		66.6	1.3	—	—	Ir(IV) Sat II
		63.5	1.3	12.8	Ir_3	Hydrous IrO_2, $Ir(OH)_3$
		64.7	1.4	—	—	Ir(III) Sat
	CoIr-CL	60.9	3.5	33.8	$Ir5p_{1/2}$	Metal, oxide and hydroxide range
		59.6	1.7	23.8	Co3p	Metal, oxide and hydroxide range
		60.9	0.9	24.3	Ir_0	Metallic iridium
		61.6	1.1	10.5	Ir_1	IrO_2
		62.5	1.2	4.2	Ir_2	Ir_2O_3, $IrCl_3 \cdot xH_2O$, $IrCl_x$ and/or $IrCl_3$
		62.9	1.0	—	—	Ir(IV) Sat I
		66.8	1.1	—	—	Ir(IV) Sat II
		63.4	1.3	3.4	Ir_3	Hydrous IrO_2, $Ir(OH)_3$
		64.8	1.4	—	—	Ir(III) Sat
O1s	IrO_2	529.8	1.55	32.4	IrO_2	IrO_2
		530.8	1.56	27.9	O_1	Ir_2O_3, $M_x(CO_3)_y$
		531.6	1.63	19.8	O_2	$Ir(OH)_3$, $IrO(OH)_2$
		532.4	1.70	13.7	O_3	$IrCl_3 \cdot xH_2O$, ClO_3^-, C–OH, C–O–C
		533.6	1.78	5.0	O_4	NO_3^-, O═C–O, OH ads. species
		534.9	1.85	1.1	O_5	–COO–, O═C–O, adsorbate
	CoIr-CL	529.4	1.33	7.5	CoO_x	CoO, Co_3O_4
		529.9	1.34	25.8	IrO_2	IrO_2
		530.9	1.40	23.9	O_1	Ir_2O_3, $M_x(CO_3)y$
		531.5	1.47	17.5	O_2	$Ir(OH)_3$, $IrO(OH)_2$
		532.3	1.53	14.5	O_3	$IrCl_3 \cdot xH_2O$, ClO_3^-, C–OH, C–O–C
		533.6	1.60	8.9	O_4	NO_3^-, O═C–O, OH ads. species
		535.2	1.66	1.9	O_5	–COO–, O═C–O, adsorbate
Co2p	CoIr-CL	776.9	2.75	7.1	Co LMM	Co Auger $L_3M_{23}M_{45}$ transition
		778.2	1.02	35.8	Co_1	Metallic cobalt
		781.6	2.52	—	—	1st metallic cobalt satellite
		783.8	2.77	—	—	2nd metallic cobalt satellite
		779.1	1.29	21.8	Co_2	Co_3O_4
		781.3	1.67	—	—	1st Co_3O_4 multiplet
		782.4	1.77	—	—	2nd Co_3O_4 multiplet
		785.5	2.44	—	—	1st Co_3O satellite
		789.5	2.91	—	—	2nd Co_3O satellite
		780.2	1.80	35.3	Co_3	$Co(OH)_2$, CoOOH, CoO
		783.4	2.69	—	—	1st $Co(OH)_2$ multiplet
		787.2	2.98	—	—	1st $Co(OH)_2$ satellite
		791.8	3.23	—	—	2nd $Co(OH)_2$ satellite

[a] Average content of six points.

after cycling to potentials required for OER, modifying the surface functional groups. Therefore, in order to have obtain a representative surface structure upon which the OER reaction takes place, an "electrochemical oxidation" step (notated with an "EO" subscript) comprising 60 scans between 0.05–1.5 V_{RHE}, was carried out with the CoIr-CL and IrO_2 catalysts. The catalyst after the EO step is labelled as CoIr-CL_{EO} (Fig. 7A, blue curve). After electrochemical oxidation, the peaks due to H_{upd} features were no longer observed, instead, two broad anodic peaks around 0.27 V_{RHE} and 0.82 V_{RHE} assigned to iridium hydroxide/oxide surface features were present.[83] The CVs of CoIr-CL_{EO} and $IrO_{2\text{-}EO}$ are compared in Fig. 7C. Within $IrO_{2,EO}$, the anodic peak at ~0.48 V_{RHE} (labeled A_0) has been attributed to formation of iridium(III) hydroxide[86] and modelled as involving the oxidation of two Ir^{3+}–OH_2 groups to two Ir^{4+}–OH groups,[87] while the peak at ~0.81 V (labeled B_0) has been attributed to oxidation of iridium(III) hydroxide to tetravalent IrO_2 or $IrO(OH)_2$.[86,88] Compared with the CV of $IrO_{2\text{-}EO}$, the CV of CoIr-CL_{EO} showed

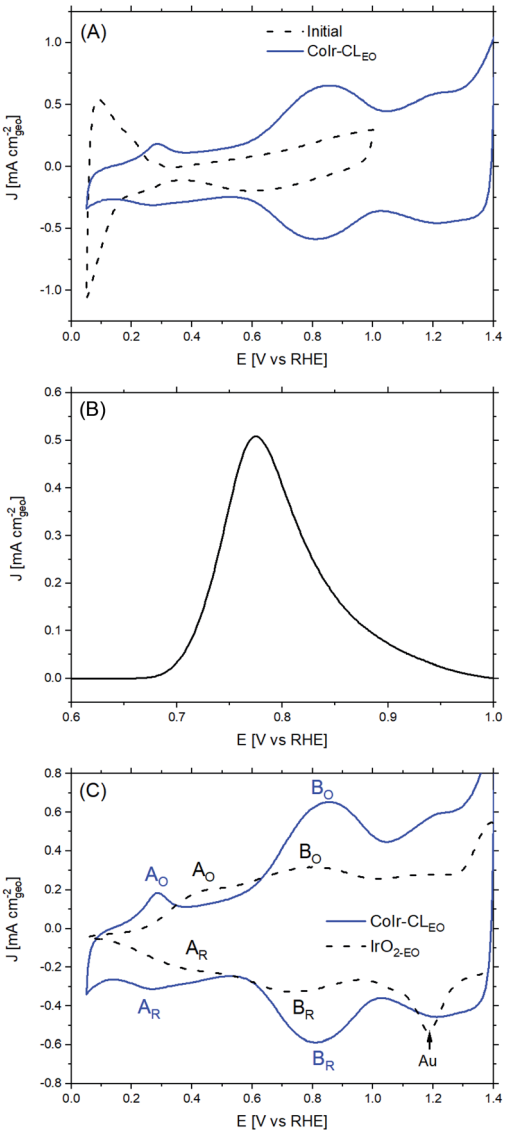

Fig. 7 (A) Cyclic voltammograms of CoIr-CL (dashed black line) and CoIr-CL_{EO}, after electrochemical oxidation, (solid blue line); (B) carbon monoxide (CO) stripping voltammetry of CoIr-CL; and (C) comparison of cyclic voltammograms of CoIr-CL_{EO} and $IrO_{2\text{-}EO}$; peaks A and B are notated as oxidation (labelled with subscript "O") or reduction (labelled with subscript "R") peaks; details provided in the text.

the anodic peak, A_0, at a significantly lower potential of ~0.27 V_{RHE} compared to the voltage of the peak at $IrO_{2\text{-}EO}$ (~0.48 V_{RHE}) which suggests different local chemical environments for hydrated Ir–OH species at the surface of CoIr-CL_{EO} and $IrO_{2\text{-}EO}$.

Since the surface of CoIr-CL_{EO} was no longer metallic after the electrochemical oxidation step, we used pseudocapacitance measurements (Fig. S8†) and previously reported parameters and conversion factors[37] to determine the ECSA of CoIr-CL_{EO} (Table S5†). The $ECSA_{IrO2}$ of CoIr-CL_{EO} determined from pseudocapacitance measurements was calculated to be 30 ± 5 m^2 g^{-1} which is much lower than the $ECSA_{Ir}$ value determined from CO stripping (61.2 ± 3.1 m^2 g^{-1}) obtained before electrochemical oxidation, but very similar to the surface area estimated for $IrO_{2\text{-}EO}$. The growth of the oxide/hydroxide surface species during the electrochemical oxidation step may result in lowering the surface area by growing within smaller pores and limiting the access of the electrolyte.[74,89] Our previous study of NiIr nanoframes showed the presence of a ~5 Å-thick oxide/hydroxide surface layer after the electrochemical oxidation step.[14]

Evaluation of electrochemical oxygen evolution activity and reaction mechanism

Following the electrochemical oxidation step, the OER activity of the CoIr-CL_{EO} catalyst material was electrochemically evaluated based on previously reported methods by our group[14] and other groups.[36] To determine the OER current, we used chronoamperometry rather than linear sweep voltammetry to reduce the contribution of electrochemical double layer capacitance.[14] To evaluate the mass activity, the current determined from chronoamperometry was normalized for the actual Ir mass which was calculated by determining the Ir mass on the electrode and subtracting the Ir leached out into the solution during the EO step determined by inductively coupled plasma mass spectrometry (details provided in Experimental section).

Shown in Fig. 8A are the chronoamperometric polarization curves of CoIr-CL_{EO} and $IrO_{2,EO}$ normalized *versus* the mass of Ir. The higher current observed for CoIr-CL_{EO} within the OER chronoamperometric curve clearly shows the superior OER activity of CoIr-CL_{EO} compared to $IrO_{2,EO}$. The mass-normalized OER activities of the CoIr-CL_{EO}, and $IrO_{2\text{-}EO}$ were compared at 1.51 V_{RHE} and are shown in Fig. 8C. A potential of 1.51 V_{RHE} was used since the Tafel plot (Fig. 8B) still shows linear behavior within this voltage region, and lower overpotential relative to the thermodynamic potential of the reaction also minimizes the contribution of mass transport. At a potential of 1.51 V_{RHE}, the mass activity of CoIr-CL_{EO} (243 ± 47 A g_{Ir}^{-1}) is 17 times higher than the mass activity of $IrO_{2\text{-}EO}$ (13.9 ± 1.4 A g_{Ir}^{-1}).

We determined the OER specific activity by normalizing the current to the electrochemical surface area determined from pseudocapacitance measurements. As shown in Fig. 8D, the OER specific activities at 1.51 V_{RHE} is 0.80 ± 0.02 A cm_{IrO2}^{-2} for CoIr-CL_{EO} which is significantly (18 times) higher than the OER specific activity of 0.045 ± 0.005 A cm_{IrO2}^{-2} for commercial IrO_2 ($IrO_{2\text{-}EO}$). The CoIr-CL_{EO} catalyst showed a significant improvement in both mass and specific OER activity compared with the commercial $IrO_{2\text{-}EO}$ catalyst.

The improvement of the specific activity of CoIr-CL_{EO} compared to $IrO_{2\text{-}EO}$ indicates that the catalytically active surface sites of CoIr-CL_{EO} are more active for oxygen evolution. Our XPS measurements (Fig. 6) support the presence of multiple species within the surface region including iridium oxide, iridium oxyhydroxide, and iridium hydroxide with iridium in 4+ and 3+ oxidation states and the presence of cobalt oxides and hydroxides with cobalt in 2+ and 3+ oxidation states. However, our CV data (Fig. 7C) shows that the surface is changed after undergoing exposure to high oxidation potentials under OER conditions, and therefore the CV measurements are more representative of the OER catalyst surface. The CV of CoIr-

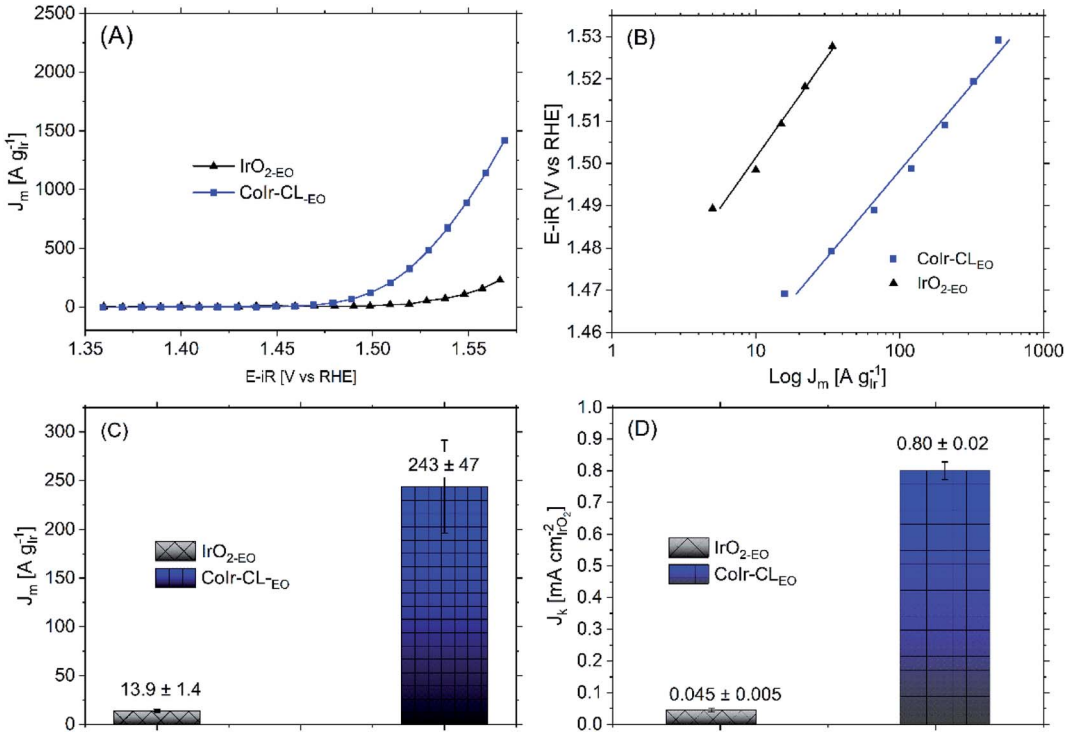

Fig. 8 (A) Current in the oxygen evolution reaction (OER) voltage region determined from chronoamperometry measurements of CoIr-CL 2D nanoframes and commercial IrO_2 after electrochemical oxidation (EO) step; testing performed in O_2-free 0.1 M $HClO_4$ under rotation at 2500 rpm; (B) Tafel plot and fitted Tafel slopes obtained from chronoamperometry data; the potential (iR-corrected) was set between 1.47 V to 1.52 V to reduce the mass transport contribution; (C) comparison of OER mass activities at 1.51 V_{RHE}; and (D) comparison of OER specific activities at 1.51 V_{RHE}.

CL_{EO} (Fig. 7C) shows peaks consistent with the surface having Ir^{3+}–OH and $Ir^{4+}O_2$ or $Ir^{4+}O(OH)_2$ groups. As discussed above, the potential of the oxidation peak at ~0.27 V_{RHE}, attributed to surface Ir^{3+}–OH groups occurs at a lower potential compared to the peak potential of ~0.48 V_{RHE} for $IrO_{2\text{-}EO}$. Prior work supports that iridium hydroxo (Ir–OH) surface species are strongly linked to OER activity,[2] and Ir–OH groups can be considered as descriptors for OER activity.[90] The higher surface activity of CoIr-CL_{EO} compared to $IrO_{2\text{-}EO}$ is attributed to presence of highly active Ir-OH species that may interact with subsurface Co; however, additional analysis is needed to characterize the surface under reaction conditions. The OER in acid involves a complex, multi-step reaction with multiple intermediates (discussed below). A number of prior studies support that at OER potentials the oxidation state of iridium increases from 4+ to 5+,[91–93] while other studies report only Ir^{4+} is present under OER conditions.[94–96] The different electronegativity of Co compared to Ir may influence the oxidation states and electron density distribution within one or more of the OER steps and/or intermediates.[2,14,90–96] Substituents influence local electron density and affect the OER steps as supported by our previous study that modelled the effect of Ni-substituted into IrO_2 and found Ni within specific sites resulted in electron density accumulation within bridging oxygens, lowering the activation energy of the rate-determining OH bond breaking step.[14] Prior DFT calculations support that cobalt doping within IrO_2 modifies the electronic structure of the active site and lowers the OER activation energy.[25] A previous study reported Co incorporation within $SrIrO_3$ increased the coverage of surface hydroxyl groups, modified the Ir–O bond covalency, altered the oxygen p-band center of the material, and increased OER activity.[30] We confirmed that cobalt remains within the structure after exposure to OER conditions following durability testing (Fig. S9†); however, additional analysis is needed to determine the specific nature of Co within the surface region after exposure to electrochemical potentials and how Co within IrO_2 affects the electron density and OER kinetics.

In addition to direct comparison of the OER activity of CoIr-CL_{EO} with $IrO_{2\text{-}EO}$ from our group's tests,[14] the OER mass activities of CoIr-CL_{EO} were compared with previously reported Co and Ir based catalysts in Table S6.† A direct comparison is difficult due to differences in the experimental conditions such as the type of electrolyte, electrochemical method (*i.e.* linear sweep voltammetry or chronoamperometry), catalyst loading, potential of the analysis, ohmic drop correction, background subtraction *etc.*, which can influence the final activity values.[14] The CoIr-CL_{EO} nanoframes showed one of the highest OER activities compared to similar CoIr-based materials reported to date only lower than recently reported IrCo nanowires.[3] The overpotential of CoIr-CL_{EO} nanoframes was also lower than that of previously reported IrCo oxide materials.[27,28]

The Tafel slopes of CoIr-CL_{EO} and $IrO_{2,EO}$ (Fig. 8B) were analyzed to provide insight regarding the reaction mechanism.[97,98] The Tafel slope of CoIr-CL_{EO} (40 ± 4 mV dec^{-1}) is

similar to the Tafel slope of $IrO_{2,EO}$ (44 ± 3 mV dec^{-1}), and consistent with the value of others that report a similar $IrO_x(OH)_y$ surface structure.[99] The similar Tafel slopes of CoIr-CL_{EO} and $IrO_{2\text{-}EO}$ suggest that similar rate-determining step is controlling the reaction mechanism on both catalysts. Previous studies on OER mechanisms have proposed different electrochemical pathways including the "electrochemical oxide path" and "DFT-predicted peroxide path", differentiated by the formation of dissimilar surface intermediate species and recombination steps.[100–103] The electrochemical oxide path is described by eqn (1)–(3) below,

$$H_2O + M \rightarrow M\text{–}OH + H^+ + e^- \quad (1)$$

$$M\text{–}OH \rightarrow M\text{–}O + H^+ + e^- \quad (2)$$

$$2M\text{–}O \rightarrow 2M + O_2 \quad (3)$$

where M describes a surface-active site. The DFT-predicted peroxide path involves the same two first initial steps as the electrochemical oxide path, eqn (1) and (2), but then involves different subsequent reaction steps, described by eqn (4) and (5) below.[103]

$$M\text{–}O + H_2O \rightarrow MOOH + H^+ + e^- \quad (4)$$

$$MOOH \rightarrow M + O_2 + H^+ + e^- \quad (5)$$

Within both reaction mechanisms (*i.e.* electrochemical oxide path and DFT-predicted peroxide path), considering the second proton–electron transfer step as the rate limiting reaction step results in a predicted Tafel slope of 40 mV dec^{-1}.[101] The measured values of the Tafel slopes of CoIr-CL_{EO} and $IrO_{2\text{-}EO}$ suggest that the OER is limited by the second electron transfer step (eqn (2)) which involves formation of Ir–O species and that the reaction may proceed *via* either the electrochemical oxide path or DFT-predicted peroxide path. It is important to note that the analysis of the reaction mechanism using the Tafel slope includes the assumption that the relative surface coverage of the adsorbed species is constant.[100] Results obtained by microkinetic analysis[98] have demonstrated that the evolution of the concentration of intermediates must be considered; therefore, more analysis needs to be done to corroborate the actual mechanism.

Evaluation of electrocatalyst stability

Within acidic OER catalysts, stability remains a critically important but significantly less studied factor relative to activity.[18,104] Catalyst degradation and long term performance have an important impact on the development of PEM electrolyzers, particularly with low catalyst loadings.[3] The stability of the catalyst was evaluated using an accelerated durability testing (ADT) protocol consisting of applying a constant potential of 1.6 V for 13.5 hours, which has been previously utilized to evaluate the durability of a number of iridium-based catalysts.[3,36]

The comparison of the iridium mass-normalized current, Tafel slopes, OER mass activities, and OER specific activities of CoIr-CL_{EO} and $IrO_{2\text{-}EO}$ (after EO) and CoIr-CL_{ADT} and $IrO_{2\text{-}ADT}$ (after ADT) are presented in Fig. 9A–D. As shown in Fig. 9A, both CoIr-CL_{EO} and $IrO_{2\text{-}EO}$ resulted in lower currents after the ADT protocol, which is consistent with prior reports of IrO_2 that showed catalyst performance degradation occurs under similar testing conditions.[36] The OER mass activity of the commercial $IrO_{2\text{-}EO}$ catalyst at 1.51 V_{RHE} decreased from 13.9 to 11.7 A g_{Ir}^{-1} indicating a retention of 84 ± 7% of the initial mass-normalized current, and the OER mass activity of the CoIr-CL_{EO} catalyst decreased from 243 to 192 A g_{Ir}^{-1} indicating a retention of 79 ± 9% of the initial mass-normalized current (Fig. 9C). After the ADT protocol, the specific activity of $IrO_{2\text{-}ADT}$ was reduced by ~7% from 0.045 ± 0.005 mA cm_{IrO2}^{-2} to 0.042 ± 0.005 mA cm_{IrO2}^{-2}, while the specific activity of CoIr-CL_{ADT} slightly increased (~4%) from 0.80 ± 0.02 mA cm_{IrO2}^{-2} to 0.83 ± 0.08 mA cm_{IrO2}^{-2}, (Fig. 9D). The analysis of the Tafel slopes of CoIr-CL_{EO} and $IrO_{2\text{-}EO}$ before and after ADT (Fig. 9B) suggests that the reaction mechanism and possibly the nature of active sites on the surface remain similar. As explained above, it is likely that the second electron transfer remains the rate determining step before and after ADT; however, more studies are needed to support the specific reaction mechanism.

To gain insight into the electrochemical stability, understand the intrinsic relationship between mass and specific activity within CoIr-CL_{ADT} and $IrO_{2\text{-}ADT}$, and evaluate the relative contributions of different factors involved in the degradation process, we further compared the surface structure, morphology, and iridium and cobalt dissolution over the ADT protocol. The mass and specific activity are related, and the relationship can be described by eqn (6),[105]

$$J_{mass} = J_k \times \frac{r_f}{L_{Ir}} \quad (6)$$

were J_{mass} represents the mass activity, J_k the specific activity, r_f the roughness factor, corresponding to the ratio of electrochemical area/geometric area (S_{IrO_2}/S_{geo}), and L_{Ir}, the loading of iridium on the electrode (μg_{Ir} cm^{-2}). Using this relationship, it can be observed that any factor affecting specific activity will also influence the mass activity. In addition, changes experienced by the catalyst that influence one or more of these parameters (*i.e.* dissolution, agglomeration, changes of morphology, changes in conductivity, and/or modification or blocking of the active sites, *etc.*), can impact mass activity and specific activity differently depending on the nature of the catalyst and how it evolves during the degradation process.

To understand factors contributing to the increase in specific activity for CoIr-CL_{ADT} and the decrease in specific activity for $IrO_{2\text{-}ADT}$, we first analyzed the evolution of the surface of the CoIr-CL and IrO_2 catalysts before and after ADT by CV (Fig. S8†). In general, the CVs of the catalysts after EO and after ADT showed qualitatively similar profiles, suggesting that the surface chemical environment remained unchanged. However, the decrease in the coulombic charge after ADT is associated to the loss of electrochemically active surface sites, either associated to dissolution of Ir or particle agglomeration. Changes in the morphology and agglomeration were demonstrated by microscopy after ADT (Fig. S9†), and the iridium

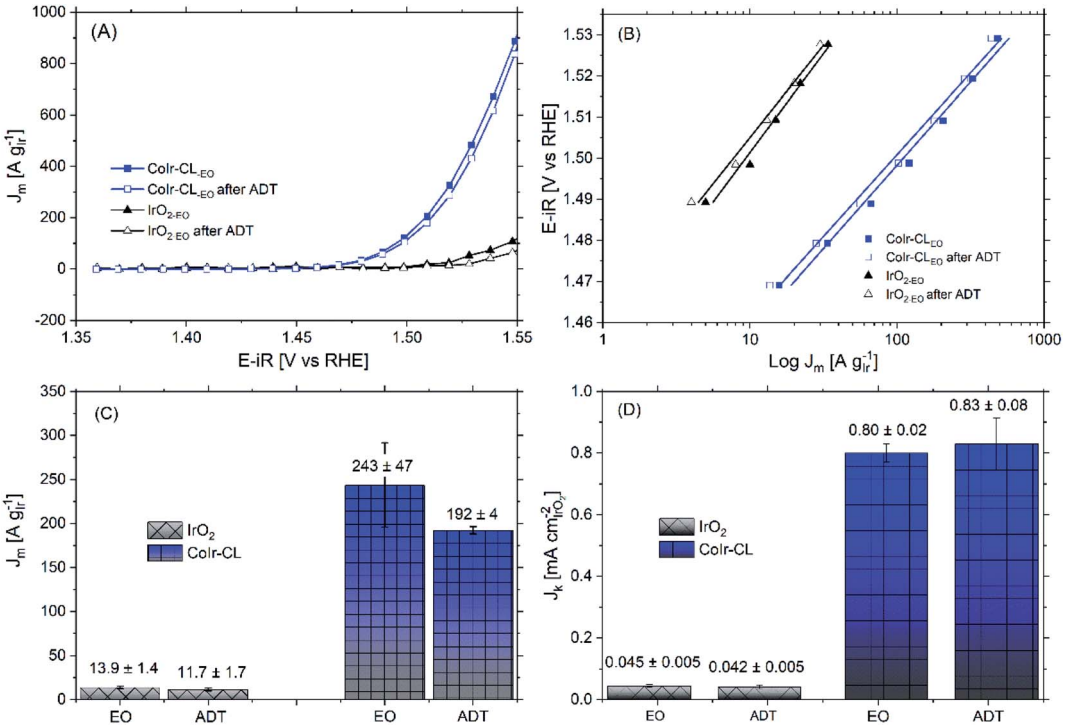

Fig. 9 (A) Current in the oxygen evolution reaction (OER) voltage region determined from chronoamperometry measurements of CoIr-CL 2D nanoframes and commercial IrO_2 before and after accelerated durability testing in O_2-free 0.1 M $HClO_4$. The stability was carried out using a potentiostatic procedure by holding the working electrode at 1.6 $V_{RHE\text{-}iR\text{-}corrected}$ for 13.5 hours under rotation at 2500 rpm; (B) Tafel plot and Tafel slopes before and after accelerated durability testing determined by chronoamperometry; the potential (iR-corrected) was set between 1.47 V to 1.52 V to minimize the mass transport contribution; (C) comparison of OER mass activities at 1.51 V_{RHE} before and after accelerated durability testing; (D) comparison of OER specific activities at 1.51 V_{RHE} before and after accelerated durability testing.

dissolution rate was determined by analyzing the concentration of Ir within the electrolyte solution after EO and ADT protocols, as discussed below.

The similarities of the Tafel slopes (Fig. 9B) and cyclic voltammograms (Fig. S8†) obtained before and after ADT discredits the idea that the changes on the nature of active sites or the reaction mechanism are primarily responsible for modifying the specific activity of CoIr-CL. Upon further examination although qualitatively the electroactive species observed within the CV seem to be the same, the relative charge of the electroactive species was determined to be different after ADT. Considering that the oxidation peak, A_o, is intimately related to the presence of highly active sites of Ir^{3+}–OH species, which have been taken as experimental descriptors toward increasing specific activity,[90] the changes of the number of these surface species are an important factor. The fitting of the CV curves allowed the quantification of the relative charge associated to the different surface species (*i.e.* Ir^{3+}–OH species,[2] and Ir^{3+} to Ir^{4+} species within an oxide structure[87,88]). The analysis of the relative ratio of coulombic charge of oxidation peaks A_o/B_o decreased from 0.12 to 0.097 for $IrO_{2\text{-}ADT}$ but increased from 0.05 to 0.085 for CoIr-CL_{ADT} (Fig. S8†). The reduction of highly active Ir^{3+}–OH species may be responsible for the reduction of activity of $IrO_{2\text{-}ADT}$, and the increase of Ir^{3+}–OH species may be responsible for improving of the specific activity of CoIr-CL_{ADT}. Additional analysis is needed to consider other factors (*e.g.* conductivity, *etc.*).

The OER mass activity is intimately related to the OER specific activity, but also to the number of iridium active sites available for the reaction, as described in eqn (6). Therefore, changes of specific activity and/or ECSA, caused by Ir dissolution or changes of morphology among other factors will affect mass activity. The OER mass activity of the commercial $IrO_{2\text{-}EO}$ catalyst at 1.51 V_{RHE} decreased from 13.9 to 11.7 A g_{Ir}^{-1} (Fig. 9A and C). The average decrease of mass activity in $IrO_{2\text{-}ADT}$ can be explained by the combined contribution of lower specific activity (~7%) and partial dissolution of Ir as discussed below.

After the ADT protocol, the OER mass activity of the CoIr-CL_{EO} catalyst at 1.51 V_{RHE} decreased from 243 to 192 A g_{Ir}^{-1} resulting in a relative stability of 79 ± 9%, which is within experimental error of the value of the commercial IrO_2 catalyst. However, at higher potential of 1.55 V_{RHE} (Table S5†), the mass activity retention of CoIr-CL_{EO} was 94 ± 2%. In contrast the $IrO_{2\text{-}EO}$ catalyst showed a relative retention of mass activity at 1.55 V_{RHE} which was lower (66 ± 9%) but within experimental error of the value at 1.51 V_{RHE} (77 ± 7%) (Table S5†). The mass transport issues become more relevant at higher current densities due to the inability to remove reaction products fast enough.[38] The improved retention of mass activity at higher voltages for the CoIr-CL_{EO} catalyst compared with commercial IrO_2 may also represent an important advantage in practical electrolyzer cells that operate at higher current densities and voltages. The post-mortem SEM analysis of the CoIr-CL_{ADT}

Table 3 Quantification of the mass loading, iridium dissolution percent loss, and iridium corrosion rate determined from the initial electrode loading and evaluation of iridium within the electrolyte determined from ICP-MS analysis after the electrochemical oxidation (EO) step and accelerated durability testing (ADT) step

	IrO_2		CoIr-CL		
	Mass loading (μg_{Ir} cm_{geo}^{-2})	Ir dissolution rate (pg_{Ir} cm^{-2} s^{-1})	Mass loading (μg_{Ir} cm_{geo}^{-2})	Ir dissolution rate (pg_{Ir} cm^{-2} s^{-1})	Co dissolution rate (pg_{Co} cm^{-2} s^{-1})
Initial	11.6	—	15.3	—	
EO	11.6	2.4[a]	13.7	997 ± 470	2990 ± 250
ADT	10.5	27.8 ± 1.6	11.0	66 ± 23	4 ± 3

[a] Value estimated from previous report.[14]

(Fig. S9†) showed the presence of cobalt, the retention of 2D-structure, and the existence of additional morphologies that included small nanoparticles. We consider that the ability of CoIr-CL_{EO} to maintain high activity after durability testing may result from the combination of (i) retention of the high specific surface activity by the presence of highly active surface functional groups and (ii) the partial retention of the integrated nanostructured morphology.

Multiple studies have shown that iridium dissolution occurs under the highly oxidative potentials and highly acidic conditions used for acidic oxygen evolution.[19,20,83] The Ir dissolution rate is also affected by the presence of non-noble metals (*i.e.* Co, Ni *etc.*) within the structure as well as the experimental processes used during the electrochemical conditioning and testing of the electrode.[3,12,14] To gain more insight into the degradation processes, we analyzed the Ir dissolution rates of IrO_2 and Ir and Co cobalt dissolution rates of CoIr-CL, both after EO and after ADT using ICP-MS analysis, and the results are summarized in Table 3. Significant differences between the dissolution rates are observed between IrO_2 and CoIr-CL and between the EO and ADT steps. For IrO_2, the EO protocol resulted in an Ir dissolution rate of 2.4 pg_{Ir} cm^{-2} s^{-1} and barely contributed to the dissolution of Ir from IrO_2 giving only 1.1 ± 0.1 wt%.[14] This result is in line with the constant CV profile observed before and after EO for commercial IrO_2 (data not shown). The ADT protocol resulted in a higher Ir dissolution rate of 27.8 ± 1.6 pg_{Ir} cm^{-2} s^{-1} for $IrO_{2\text{-ADT}}$. The dissolution of Ir has been shown to be potential-dependent,[83] and the different Ir dissolution rates of IrO_2 for EO and ADT steps may result from the different protocols that involve either potential sweeps (EO step) or constant potentials (ADT).

For the CoIr-CL_{EO} catalyst, the EO step involves a high rate of Ir dissolution (997 ± 470 pg_{Ir} cm^{-2} s^{-1}) and Co dissolution (2990 ± 250 pg_{Co} cm^{-2} s^{-1}) into the solution (Table 3) which can be explained by the significant surface reorganization involved in the EO step that transforms the initially metallic surface to an oxide/hydroxide surface (Fig. 7A). It is possible that the Ir and Co dissolution during the EO step may contribute to the generation of highly active Ir–OH groups. A previous study reported leaching of nickel from Ir–Ni oxide thin films resulted in formation of highly active Ir–OH surface sites.[12] The higher dissolution rate of Ir within CoIr-CL_{EO} compared to $IrO_{2\text{-EO}}$ is consistent with our prior study of hydrous nickel–iridium oxide OER catalysts where presence of Ni increased the dissolution of iridium compared to IrO_2.[14] CoIr-CL_{ADT} showed a significant reduction of the iridium corrosion rate to 66 ± 23 pg_{Ir} cm^{-2} s^{-1} compared to the value after the EO step (997 ± 470 pg_{Ir} cm^{-2} s^{-1}). After the significant surface reorganization and dissolution involved in the potential sweeps of the EO step of CoIr-CL, the catalyst surface may then become passivated resulting in lower dissolution of Ir and Co over the ADT step, which is supported by the comparison of the CVs for the EO step and ADT step (Fig. S8†). However, the iridium corrosion rate for CoIr-CL_{ADT} still showed a ~2 times higher dissolution rate compared to $IrO_{2\text{-ADT}}$.

The comparison of the electrochemical stabilities of CoIr-CL and IrO_2 shows significantly different degradation processes occur for these materials. While from an application perspective additional work is needed to further reduce Ir dissolution rate, despite the higher iridium dissolution of CoIr-CL_{ADT}, the increase in the relative concentration of surface Ir–OH groups and the presence of Co within the sublayers resulted in an increase of the specific activity and the retention of OER mass activities compared with IrO_2.

Conclusions

Cobalt–iridium two-dimensional nanoframes were synthesized by thermal reduction of iridium-decorated cobalt hydroxide nanosheets followed by a chemical leaching step in acid. The synthesis process resulted in interconnected Co–Ir alloy domains within an unsupported, carbon-free porous nanostructure that allows three-dimensional molecular access to the catalytically active surface sites. After electrochemical conditioning within the OER potential range, the predominately bimetallic alloy surface was transformed to oxide/hydroxide surface. Oxygen evolution activities determined using rotating disk electrode configuration showed that hydrous Co–Ir oxide nanoframes showed 17 times higher OER mass activity and 18 times higher OER specific activity compared with commercial IrO_2. The higher OER activities are attributed to the presence of highly active iridium hydroxide surface species within the hydrous Co–Ir oxide surface and subsurface Co–Ir alloy that tunes the surface atomic and electronic structure. CV measurements show the presence of an anodic iridium hydroxide peak at lower potential compared with IrO_2 which

supports the Co–Ir nanoframes have highly active Ir–OH surface species that may contribute to the high OER activity.

In addition to higher activity, the hydrous Co–Ir oxide nanoframes exhibited similar retention of initial OER mass activity (79 ± 9% retention) as commercial IrO_2 (84 ± 7% retention) tested with rotating disk electrode measurements using an accelerated durability testing protocol. The retention of OER mass activity over accelerated durability testing of cobalt-containing Co–Ir nanoframes was dramatically higher than similarly prepared nickel-containing Ni–Ir nanoframes[14] which suggests cobalt–iridium interaction may be more stable than nickel–iridium interaction within these structures. The comparison of the factors influencing the electrochemical stabilities of CoIr-CL and IrO_2 under OER conditions indicates that the catalysts undergo significantly different degradation processes. The decrease in the OER mass activity of the IrO_2 catalyst can be explained by the combined contribution of lower specific activity and partial dissolution of Ir. The analysis of the degradation of hydrous Co–Ir oxide nanoframes showed a higher Ir dissolution rate for the compared with IrO_2; however, the specific activity of CoIr-CL_{EO} and the relative contribution of surface iridium hydroxide groups increased which contributes to the similar OER mass stability of CoIr-CL_{EO} compared with IrO_2 under the ADT testing conditions. Our work that shows that the bimetallic cobalt–iridium 2D nanoframes obtain a significantly higher OER mass activity and similar stability compared with a commercial benchmark IrO_2; however, the bimetallic Co–Ir catalyst undergoes a significantly different degradation process compared with the monometallic IrO_2 catalyst. Our work furthers the understanding of factors influencing the activity and stability of bimetallic and monometallic acidic OER electrocatalysts and contributes to the design of electrocatalysts with high activity and stability.

Conflicts of interest

There are no conflicts to declare.

Acknowledgements

The authors acknowledge support of this research from the Office of Naval Research Grant No. N00014-16-1-2777 and N00014-19-1-2071 for materials, structural and electrochemical characterization. The authors acknowledge support of this research from the National Science Foundation Award No. 1936458 for stability and dissolution analysis. R. M. acknowledges support from the National Science Foundation Research Experiences for Undergraduates (REU) Award, Grant No. 1757843. The authors would like to thank Dr Sanmathi Chavalmane Subbenaik (Washington University in Saint Louis) for her assistance in obtaining ICP-MS analysis.

References

1 M. Carmo, D. L. Fritz, J. Mergel and D. Stolten, A Comprehensive Review on PEM Water Electrolysis, *Int. J. Hydrogen Energy*, 2013, **38**, 4901–4934.
2 D. F. Abbott, D. Lebedev, K. Waltar, M. Povia, M. Nachtegaal, E. Fabbri, C. Copéret and T. J. Schmidt, Iridium Oxide for the Oxygen Evolution Reaction: Correlation between Particle Size, Morphology, and the Surface Hydroxo Layer from Operando XAS, *Chem. Mater.*, 2016, **28**, 6591–6604.
3 S. M. Alia, S. Shulda, C. Ngo, S. Pylypenko and B. S. Pivovar, Iridium-Based Nanowires as Highly Active, Oxygen Evolution Reaction Electrocatalysts, *ACS Catal.*, 2018, **8**, 2111–2120.
4 T. J. Meyer, The Art of Splitting Water, *Nature*, 2008, **451**, 778.
5 N. Danilovic, R. Subbaraman, K.-C. Chang, S. H. Chang, Y. J. Kang, J. Snyder, A. P. Paulikas, D. Strmcnik, Y.-T. Kim, D. Myers, V. R. Stamenkovic and N. M. Markovic, Activity–Stability Trends for the Oxygen Evolution Reaction on Monometallic Oxides in Acidic Environments, *J. Phys. Chem. Lett.*, 2014, **5**, 2474–2478.
6 M. H. Miles and M. A. Thomason, Periodic Variations of Overvoltages for Water Electrolysis in Acid Solutions from Cyclic Voltammetric Studies, *J. Electrochem. Soc.*, 1976, **123**, 1459–1461.
7 T. Reier, M. Oezaslan and P. Strasser, Electrocatalytic Oxygen Evolution Reaction (OER) on Ru, Ir, and Pt Catalysts: A Comparative Study of Nanoparticles and Bulk Materials, *ACS Catal.*, 2012, **2**, 1765–1772.
8 S. Hackwood, L. M. Schiavone, W. C. Dautremont-Smith and G. Beni, Anodic Evolution of Oxygen on Sputtered Iridium Oxide Films, *J. Electrochem. Soc.*, 1981, **128**, 2569–2573.
9 H. R. Yu, N. Danilovic, Y. Wang, W. Willis, A. Poozhikunnath, L. Bonville, C. Capuano, K. Ayers and R. Maric, Nano-size IrO_x Catalyst of High Activity and Stability in PEM Water Electrolyzer with Ultra-low Iridium Loading, *Appl. Catal., B*, 2018, **239**, 133–146.
10 S. Zhao, A. Stocks, B. Rasimick, K. More and H. Xu, Highly Active, Durable Dispersed Iridium Nanocatalysts for PEM Water Electrolyzers, *J. Electrochem. Soc.*, 2018, **165**, F82–F89.
11 H. S. Oh, H. N. Nong, T. Reier, A. Bergmann, M. Gliech, J. F. de Araujo, E. Willinger, R. Schlogl, D. Teschner and P. Strasser, Electrochemical Catalyst-Support Effects and Their Stabilizing Role for IrO_x Nanoparticle Catalysts during the Oxygen Evolution Reaction, *J. Am. Chem. Soc.*, 2016, **138**, 12552–12563.
12 T. Reier, Z. Pawolek, S. Cherevko, M. Bruns, T. Jones, D. Teschner, S. Selve, A. Bergmann, H. N. Nong, R. Schlögl, K. J. J. Mayrhofer and P. Strasser, Molecular Insight in Structure and Activity of Highly Efficient, Low-Ir Ir–Ni Oxide Catalysts for Electrochemical Water Splitting (OER), *J. Am. Chem. Soc.*, 2015, **137**, 13031–13040.
13 C. Wang, R. B. Moghaddam and S. H. Bergens, Active, Simple Iridium-Copper Hydrous Oxide Electrocatalysts for Water Oxidation, *J. Phys. Chem. C*, 2017, **121**, 5480–5486.
14 F. Godínez-Salomón, L. Albiter, S. M. Alia, B. S. Pivovar, L. E. Camacho-Forero, P. B. Balbuena, R. Mendoza-Cruz, M. J. Arellano-Jimenez and C. P. Rhodes, Self-Supported Hydrous Iridium–Nickel Oxide Two-Dimensional

Nanoframes for High Activity Oxygen Evolution Electrocatalysts, *ACS Catal.*, 2018, **8**, 10498–10520.

15 J. Rossmeisl, Z. W. Qu, H. Zhu, G. J. Kroes and J. K. Norskov, Electrolysis of Water on Oxide Surfaces, *J. Electroanal. Chem.*, 2007, **607**, 83–89.

16 H. N. Nong, H.-S. Oh, T. Reier, E. Willinger, M.-G. Willinger, V. Petkov, D. Teschner and P. Strasser, Oxide-Supported $IrNiO_x$ Core–Shell Particles as Efficient, Cost-Effective, and Stable Catalysts for Electrochemical Water Splitting, *Angew. Chem., Int. Ed.*, 2015, **54**, 2975–2979.

17 W. Sun, Y. Song, X.-Q. Gong, L.-M. Cao and J. Yang, An Efficiently Tuned d-orbital Occupation of IrO_2 by Doping with Cu for Enhancing the Oxygen Evolution Reaction Activity, *Chem. Sci.*, 2015, **6**, 4993–4999.

18 C. Spori, J. T. H. Kwan, A. Bonakdarpour, D. P. Wilkinson and P. Strasser, The Stability Challenges of Oxygen Evolving Catalysts: Towards a Common Fundamental Understanding and Mitigation of Catalyst Degradation, *Angew. Chem., Int. Ed.*, 2017, **56**, 5994–6021.

19 S. Geiger, O. Kasian, M. Ledendecker, E. Pizzutilo, A. M. Mingers, W. T. Fu, O. Diaz-Morales, Z. Z. Li, T. Oellers, L. Fruchter, A. Ludwig, K. J. J. Mayrhofer, M. T. M. Koper and S. Cherevko, The Stability Number as a Metric for Electrocatalyst Stability Benchmarking, *Nat. Catal.*, 2018, **1**, 508–515.

20 Y. T. Kim, P. P. Lopes, S. A. Park, A. Y. Lee, J. Lim, H. Lee, S. Back, Y. Jung, N. Danilovic, V. Stamenkovic, J. Erlebacher, J. Snyder and N. M. Markovic, Balancing Activity, Stability and Conductivity of Nanoporous Core-shell Iridium/Iridium Oxide Oxygen Evolution Catalysts, *Nat. Commun.*, 2017, **8**, 1449.

21 M. Pourbaix, *Atlas of Electrochemical Equilibria in Aqueous Solutions*, National Association of Corrosion Engineers, Houston, Texas, 1974.

22 O. Kasian, J. P. Grote, S. Geiger, S. Cherevko and K. J. J. Mayrhofer, The Common Intermediates of Oxygen Evolution and Dissolution Reactions during Water Electrolysis on Iridium, *Angew. Chem., Int. Ed.*, 2018, **57**, 2488–2491.

23 C. Roy, R. R. Rao, K. A. Stoerzinger, J. Hwang, J. Rossmeisl, I. Chorkendorff, Y. Shao-Horn and I. E. L. Stephens, Trends in Activity and Dissolution on RuO_2 under Oxygen Evolution Conditions: Particles versus Well-Defined Extended Surfaces, *ACS Energy Lett.*, 2018, **3**, 2045–2051.

24 S.-A. Park, K.-S. Kim and Y.-T. Kim, Electrochemically Activated Iridium Oxide Black as Promising Electrocatalyst Having High Activity and Stability for Oxygen Evolution Reaction, *ACS Energy Lett.*, 2018, **3**, 1110–1115.

25 R. G. Gonzalez-Huerta, G. Ramos-Sanchez and P. B. Balbuena, Oxygen Evolution in Co-doped RuO_2 and IrO_2: Experimental and Theoretical Insights to Diminish Electrolysis Overpotential, *J. Power Sources*, 2014, **268**, 69–76.

26 J. Feng, F. Lv, W. Zhang, P. Li, K. Wang, C. Yang, B. Wang, Y. Yang, J. Zhou, F. Lin, G.-C. Wang and S. Guo, Iridium-Based Multimetallic Porous Hollow Nanocrystals for Efficient Overall-Water-Splitting Catalysis, *Adv. Mater.*, 2017, **29**, 1703798.

27 W. Hu, H. Zhong, W. Liang and S. Chen, Ir-surface Enriched Porous Ir-Co Oxide Hierarchical Architecture for High Performance Water Oxidation in Acidic Media, *ACS Appl. Mater. Interfaces*, 2014, **6**, 12729–12736.

28 W. Q. Zaman, Z. Wang, W. Sun, Z. Zhou, M. Tariq, L. Cao, X.-Q. Gong and J. Yang, Ni–Co Codoping Breaks the Limitation of Single-Metal-Doped IrO_2 with Higher Oxygen Evolution Reaction Performance and Less Iridium, *ACS Energy Lett.*, 2017, **2**, 2786–2793.

29 W. Q. Zaman, W. Sun, Z. H. Zhou, Y. Y. Wu, L. M. Cao and J. Yang, Anchoring of IrO_2 on One-Dimensional Co_3O_4 Nanorods for Robust Electrocatalytic Water Splitting in an Acidic Environment, *ACS Appl. Energy Mater.*, 2018, **1**, 6374–6380.

30 L. Yang, H. Chen, L. Shi, X. T. Li, X. F. Chu, W. Chen, N. Li and X. X. Zou, Enhanced Iridium Mass Activity of 6H-Phase, Ir-Based Perovskite with Nonprecious Incorporation for Acidic Oxygen Evolution Electrocatalysis, *ACS Appl. Mater. Interfaces*, 2019, **11**, 42006–42013.

31 S. Choi, J. Park, M. K. Kabiraz, Y. Hong, T. Kwon, T. Kim, A. Oh, H. Baik, M. Lee, S. M. Paek, S. I. Choi and K. Lee, Pt Dopant: Controlling the Ir Oxidation States toward Efficient and Durable Oxygen Evolution Reaction in Acidic Media, *Adv. Funct. Mater.*, 2020, **30**, 2003935.

32 J. Park, Y. J. Sa, H. Baik, T. Kwon, S. H. Joo and K. Lee, Iridium-Based Multimetallic Nanoframe@Nanoframe Structure: An Efficient and Robust Electrocatalyst toward Oxygen Evolution Reaction, *ACS Nano*, 2017, **11**, 5500–5509.

33 S. Cherevko, T. Reier, A. R. Zeradjanin, Z. Pawolek, P. Strasser and K. J. J. Mayrhofer, Stability of Nanostructured Iridium Oxide Electrocatalysts During Oxygen Evolution Reaction in Acidic Environment, *Electrochem. Commun.*, 2014, **48**, 81–85.

34 F. Godinez-Salomon, R. Mendoza-Cruz, M. J. Arellano-Jimenez, M. Jose-Yacaman and C. P. Rhodes, Metallic Two-Dimensional Nanoframes: Unsupported Hierarchical Nickel-Platinum Alloy Nanoarchitectures with Enhanced Electrochemical Oxygen Reduction Activity and Stability, *ACS Appl. Mater. Interfaces*, 2017, **9**, 18660–18674.

35 F. Godínez-Salomón, L. Albiter, R. Mendoza-Cruz and C. P. Rhodes, Bimetallic Two-dimensional Nanoframes: High Activity Acidic Bifunctional Oxygen Reduction and Evolution Electrocatalysts, *ACS Appl. Energy Mater.*, 2020, **3**, 2404–2421.

36 S. M. Alia, B. Rasimick, C. Ngo, K. C. Neyerlin, S. S. Kocha, S. Pylypenko, H. Xu and B. S. Pivovar, Activity and Durability of Iridium Nanoparticles in the Oxygen Evolution Reaction, *J. Electrochem. Soc.*, 2016, **163**, F3105–F3112.

37 S. Zhao, H. Yu, R. Maric, N. Danilovic, C. B. Capuano, K. E. Ayers and W. E. Mustain, Calculating the Electrochemically Active Surface Area of Iridium Oxide in Operating Proton Exchange Membrane Electrolyzers, *J. Electrochem. Soc.*, 2015, **162**, F1292–F1298.

38 H. A. El-Sayed, A. Weiss, L. F. Olbrich, G. P. Putro and H. A. Gasteiger, OER Catalyst Stability Investigation Using

RDE Technique: A Stability Measure or an Artifact?, *J. Electrochem. Soc.*, 2019, **166**, F458–F464.

39 J. Yang, H. Liu, W. N. Martens and R. L. Frost, Synthesis and Characterization of Cobalt Hydroxide, Cobalt Oxyhydroxide, and Cobalt Oxide Nanodiscs, *J. Phys. Chem. C*, 2010, **114**, 111–119.

40 D. S. Hall, D. J. Lockwood, C. Bock and B. R. MacDougall, Nickel Hydroxides and Related Materials: A Review of their Structures, Synthesis and Properties, *Proc. R. Soc. A*, 2015, **471**, 21740792.

41 H. J. Yin and Z. Y. Tang, Ultrathin Two-Dimensional Layered Metal Hydroxides: An Emerging Platform for Advanced Catalysis, Energy Conversion and Storage, *Chem. Soc. Rev.*, 2016, **45**, 4873–4891.

42 L. S. Sarma, C. H. Chen, S. M. S. Kumar, G. R. Wang, S. C. Yen, D. G. Liu, H. S. Sheu, K. L. Yu, M. T. Tang, J. F. Lee, C. Bock, K. H. Chen and B. J. Hwang, Formation of Pt-Ru nanoparticles in ethylene glycol solution: An in situ X-ray absorption spectroscopy study, *Langmuir*, 2007, **23**, 5802–5809.

43 J. Quinson, M. Inaba, S. Neumann, A. A. Swane, J. Bucher, S. B. Simonsen, L. T. Kuhn, J. J. K. Kirkensgaard, K. M. O. Jensen, M. Oezaslan, S. Kunz and M. Arenz, Investigating Particle Size Effects in Catalysis by Applying a Size-Controlled and Surfactant-Free Synthesis of Colloidal Nanoparticles in Alkaline Ethylene Glycol: Case Study of the Oxygen Reduction Reaction on Pt, *ACS Catal.*, 2018, **8**, 6627–6635.

44 V. Pecharsky and P. Zavalij, *Fundamentals of Powder Diffraction and Structural Characterization of Materials*, 2nd edn, Springer Science+Business Media, LLC, New York, 2009.

45 S. M. Londono-Restrepo, R. Jeronimo-Cruz, B. M. Milian-Malo, E. M. Rivera-Munoz and M. E. Rodriguez-Garcia, Effect of the Nano Crystal Size on the X-ray Diffraction Patterns of Biogenic Hydroxyapatite from Human, Bovine, and Porcine Bones, *Sci. Rep.*, 2019, **9**, 12.

46 P. V. Kamath and S. Ganguly, Infrared Spectroscopic Studies of the Oxide-hydroxides of Ni, Co and Mn, *Mater. Lett.*, 1991, **10**, 537–539.

47 G. Soler-Illia, M. Jobbagy, A. E. Regazzoni and M. A. Blesa, Synthesis of Nickel Hydroxide by Homogeneous Alkalinization. Precipitation Mechanism, *Chem. Mat.*, 1999, **11**, 3140–3146.

48 Z. P. Xu and H. C. Zeng, Interconversion of Brucite-like and Hydrotalcite-like Phases in Cobalt Hydroxide Compounds, *Chem. Mater.*, 1999, **11**, 67–74.

49 P. Jeevanandam, Y. Koltypin and A. Gedanken, Synthesis of Nanosized α-Nickel Hydroxide by a Sonochemical Method, *Nano Lett.*, 2001, **1**, 263–266.

50 Z. P. Liu, R. Z. Ma, M. Osada, K. Takada and T. Sasaki, Selective and Controlled Synthesis of α- and β-Cobalt Hydroxides in Highly Developed Hexagonal Platelets, *J. Am. Chem. Soc.*, 2005, **127**, 13869–13874.

51 B. Mavis and M. Akinc, Kinetics of Urea Decomposition in the Presence of Transition Metal Ions: Ni^{2+}, *J. Am. Ceram. Soc.*, 2006, **89**, 471–477.

52 L. P. Xu, Y. S. Ding, C. H. Chen, L. L. Zhao, C. Rimkus, R. Joesten and S. L. Suib, 3D Flowerlike α-Nickel Hydroxide with Enhanced Electrochemical Activity Synthesized by Microwave-assisted Hydrothermal Method, *Chem. Mater.*, 2008, **20**, 308–316.

53 Z. A. Hu, Y. L. Xie, Y. X. Wang, L. J. Xie, G. R. Fu, X. Q. Jin, Z. Y. Zhang, Y. Y. Yang and H. Y. Wu, Synthesis of α-Cobalt Hydroxides with Different Intercalated Anions and Effects of Intercalated Anions on Their Morphology, Basal Plane Spacing, and Capacitive Property, *J. Phys. Chem. C*, 2009, **113**, 12502–12508.

54 Z. F. Zhu, N. Wei, H. Liu and Z. L. He, Microwave-assisted Hydrothermal Synthesis of $Ni(OH)_2$ Architectures and their in situ Thermal Convention to NiO, *Adv. Powder Technol.*, 2011, **22**, 422–426.

55 T. Wu and C. Z. Yuan, Facile One-pot Strategy Synthesis of Ultrathin α-$Co(OH)_2$ Nanosheets Towards High-performance Electrochemical Capacitors, *Mater. Lett.*, 2012, **85**, 161–163.

56 A. K. Mondal, D. W. Su, S. Q. Chen, J. Q. Zhang, A. S. Ung and G. X. Wang, Microwave-assisted Synthesis of Spherical β-$Ni(OH)_2$ Superstructures for Electrochemical Capacitors with Excellent Cycling Stability, *Chem. Phys. Lett.*, 2014, **610**, 115–120.

57 J. T. Mehrabad, M. Aghazadeh, M. G. Maragheh, M. R. Ganjali and P. Norouzi, α-$Co(OH)_2$ Nanoplates with Excellent Supercapacitive Performance: Electrochemical Preparation and Characterization, *Mater. Lett.*, 2016, **184**, 223–226.

58 B. Pejova, A. Isahi, M. Najdoski and I. Grozdanov, Fabrication and Characterization of Nanocrystalline Cobalt Oxide Thin Films, *Mater. Res. Bull.*, 2001, **36**, 161–170.

59 J. Ismail, M. F. Ahmed, P. V. Kamath, G. N. Subbanna, S. Uma and J. Gopalakrishnan, Organic Additive-Mediated Synthesis of Novel Cobalt(II) Hydroxides, *J. Solid State Chem.*, 1995, **114**, 550–555.

60 Y. Zhang, Y. Yang, L. Yu, X. Q. Meng, F. Wen, J. L. Zhang, H. P. Bi, X. Wang and J. W. Zhu, A Facile Solvent Regulated Method for Phase Control of Two-Dimensional Nickel-Cobalt Hydroxide Nanosheets: Towards Improved Performance Hybrid Supercapacitors, *Mater. Chem. Phys.*, 2018, **218**, 172–181.

61 M. Dixit, G. N. Subbanna and P. V. Kamath, Homogeneous Precipitation from Solution by Urea Hydrolysis: A Novel Chemical Route to the α-hydroxides of Nickel and Cobalt, *J. Mater. Chem.*, 1996, **6**, 1429–1432.

62 B. Mavis and M. Akinc, Cyanate Intercalation in Nickel Hydroxide, *Chem. Mater.*, 2006, **18**, 5317–5325.

63 Q. D. Wu, X. P. Gao, G. R. Li, G. L. Pan, T. Y. Yan and H. Y. Zhu, Microstructure and Electrochemical Properties of Al-substituted Nickel Hydroxides Modified with CoOOH Nanoparticles, *J. Phys. Chem. C*, 2007, **111**, 17082–17087.

64 D. S. Hall, D. J. Lockwood, S. Poirier, C. Bock and B. R. MacDougall, Raman and Infrared Spectroscopy of α and β Phases of Thin Nickel Hydroxide Films

Electrochemically Formed on Nickel, *J. Phys. Chem. A*, 2012, **116**, 6771–6784.

65 D. S. Hall, D. J. Lockwood, S. Poirier, C. Bock and B. R. MacDougall, Applications of in Situ Raman Spectroscopy for Identifying Nickel Hydroxide Materials and Surface Layers during Chemical Aging, *ACS Appl. Mater. Interfaces*, 2014, **6**, 3141–3149.

66 W. Sawodny, K. Niedenzu and J. W. Dawson, The Vibrational Spectrum of Ethylene Glycol, *Spectrochim. Acta, Part A*, 1967, **23A**, 799–806.

67 S. B. Yang, X. L. Wu, C. L. Chen, H. L. Dong, W. P. Hu and X. K. Wang, Spherical α-$Ni(OH)_2$ Nanoarchitecture Grown on Graphene as Advanced Electrochemical Pseudocapacitor Materials, *Chem. Commun.*, 2012, **48**, 2773–2775.

68 K. Nakamoto, *Infrared Spectra of Inorganic and Coordination Compounds*, John Wiley & Sons, New York, 1963.

69 D. N. Sathyanarayana, *Vibrational Spectroscopy: Theory and Applications*, New Age International, New Dehli, 2015.

70 S. Music, S. Popovic, M. Maljkovic, Z. Skoko, K. Furic and A. Gajovic, Thermochemical formation of IrO_2 and Ir, *Mater. Lett.*, 2003, **57**, 4509–4514.

71 S. A. Makhlouf, Z. H. Bakr, K. I. Aly and M. S. Moustafa, Structural, Electrical and Optical Properties of Co_3O_4 Nanoparticles, *Superlattices Microstruct.*, 2013, **64**, 107–117.

72 P. L. Lang and L. J. Richwine, in *Practical Sampling Techniques of Infrared Analysis*, ed. P. B. Coleman, CRC Press, New York, NY, 1993, pp. 145–164.

73 M. Salavati-Niasari, A. Khansari and F. Davar, Synthesis and Characterization of Cobalt Oxide Nanoparticles by Thermal Treatment Process, *Inorg. Chim. Acta*, 2009, **362**, 4937–4942.

74 D. R. Rolison, Catalytic Nanoarchitectures - The Importance of Nothing and the Unimportance of Periodicity, *Science*, 2003, **299**, 1698–1701.

75 T. Binninger, R. Mohamed, K. Waltar, E. Fabbri, P. Levecque, R. Kotz and T. J. Schmidt, Thermodynamic Explanation of the Universal Correlation Between Oxygen Evolution Activity and Corrosion of Oxide Catalysts, *Sci. Rep.*, 2015, **5**, 12167.

76 S. C. Petitto, E. M. Marsh, G. A. Carson and M. A. Langell, Cobalt Oxide Surface Chemistry: The Interaction of CoO(100), Co_3O_4(110) and Co_3O_4(111) with Oxygen and Water, *J. Mol. Catal. A: Chem.*, 2008, **281**, 49–58.

77 A. Younis, D. W. Chu, X. Lin, J. Lee and S. Li, Bipolar Resistive Switching in p-Type Co_3O_4 Nanosheets Prepared by Electrochemical Deposition, *Nanoscale Res. Lett.*, 2013, **8**, 36.

78 M. C. Biesinger, B. P. Payne, A. P. Grosvenor, L. W. M. Lau, A. R. Gerson, R. S. Smart and R. S. Smart, Resolving Surface Chemical States in XPS Analysis of First Row Transition Metals, Oxides and Hydroxides: Cr, Mn, Fe, Co and Ni, *Appl. Surf. Sci.*, 2011, **257**, 2717–2730.

79 M. Behazin, M. C. Biesinger, J. J. Noel and J. C. Wren, Comparative Study of Film Formation on High-Purity Co and Stellite-6: Probing the Roles of a Chromium Oxide Layer and γ-Radiation, *Corros. Sci.*, 2012, **63**, 40–50.

80 D. Cabrera-German, G. Gomez-Sosa and A. Herrera-Gomez, Accurate Peak Fitting and Subsequent Quantitative Composition Analysis of the Spectrum of Co 2p Obtained with Al K Radiation: I: Cobalt Spinel, *Surf. Interface Anal.*, 2016, **48**, 252–256.

81 N. G. Farr and H. J. Griesser, XPS Excitation Dependence of Measured Cobalt 2p Peak Intensity Due to Auger Peak Interference, *J. Electron Spectrosc. Relat. Phenom.*, 1989, **49**, 293–302.

82 U. A. Paulus, T. J. Schmidt, H. A. Gasteiger and R. J. Behm, Oxygen Reduction on a High-Surface Area Pt/Vulcan Carbon Catalyst: A Thin-Film Rotating Ring-Disk Electrode Study, *J. Electroanal. Chem.*, 2001, **495**, 134–145.

83 S. Cherevko, S. Geiger, O. Kasian, A. Mingers and K. J. J. Mayrhofer, Oxygen Evolution Activity and Stability of Iridium in Acidic Media. Part 1. Metallic Iridium, *J. Electroanal. Chem.*, 2016, **773**, 69–78.

84 F. Godínez-Salomón, C. P. Rhodes, K. S. Alcantara, Q. Zhu, S. E. Canton, H. A. Calderon, J. L. Reyes-Rodríguez, M. A. Leyva and O. Solorza-Feria, Tuning the Oxygen Reduction Activity and Stability of $Ni(OH)_2$@Pt/C Catalysts through Controlling Pt Surface Composition, Strain, and Electronic Structure, *Electrochim. Acta*, 2017, **247**, 958–969.

85 S. M. Alia, K. E. Hurst, S. S. Kocha and B. S. Pivovar, Mercury Underpotential Deposition to Determine Iridium and Iridium Oxide Electrochemical Surface Areas, *J. Electrochem. Soc.*, 2016, **163**, F3051–F3056.

86 R. Kötz, H. Neff and S. Stucki, Anodic Iridium Oxide Films: XPS Studies of Oxidation State Changes and O_2 Evolution, *J. Electrochem. Soc.*, 1984, **131**, 72–77.

87 P. Steegstra, M. Busch, I. Panas and E. Ahlberg, Revisiting the Redox Properties of Hydrous Iridium Oxide Films in the Context of Oxygen Evolution, *J. Phys. Chem. C*, 2013, **117**, 20975–20981.

88 S. Cherevko, S. Geiger, O. Kasian, A. Mingers and K. J. J. Mayrhofer, Oxygen Evolution Activity and Stability of Iridium in Acidic Media. Part 2. Electrochemically Grown Hydrous Iridium Oxide, *J. Electroanal. Chem.*, 2016, **774**, 102–110.

89 J. Koresh and A. Soffer, Double Layer Capacitance and Charging Rate of Ultramicroporous Carbon Electrodes, *J. Electrochem. Soc.*, 1977, **124**, 1379–1385.

90 C. Spori, P. Briois, H. N. Nong, T. Reier, A. Billard, S. Kuhl, D. Teschner and P. Strasser, Experimental Activity Descriptors for Iridium-Based Catalysts for the Electrochemical Oxygen Evolution Reaction (OER), *ACS Catal.*, 2019, **9**, 6653–6663.

91 H. G. S. Casalongue, M. L. Ng, S. Kaya, D. Friebel, H. Ogasawara and A. Nilsson, In Situ Observation of Surface Species on Iridium Oxide Nanoparticles during the Oxygen Evolution Reaction, *Angew. Chem., Int. Ed.*, 2014, **53**, 7169–7172.

92 Y. B. Mo, I. C. Stefan, W. B. Cai, J. Dong, P. Carey and D. A. Scherson, In situ iridium L-III-edge X-ray absorption and surface enhanced Raman spectroscopy of electrodeposited iridium oxide films in aqueous electrolytes, *J. Phys. Chem. B*, 2002, **106**, 3681–3686.

93 A. Minguzzi, O. Lugaresi, E. Achilli, C. Locatelli, A. Vertova, P. Ghigna and S. Rondinini, Observing the Oxidation State Turnover in Heterogeneous Iridium-based Water Oxidation Catalysts, *Chem. Sci.*, 2014, **5**, 3591–3597.

94 V. Pfeifer, T. E. Jones, J. J. V. Velez, R. Arrigo, S. Piccinin, M. Havecker, A. Knop-Gericke and R. Schlogl, In Situ Observation of Reactive Oxygen Species Forming on Oxygen-Evolving Iridium Surfaces, *Chem. Sci.*, 2017, **8**, 2143–2149.

95 P. Lettenmeier, J. Majchel, L. Wang, V. A. Saveleva, S. Zafeiratos, E. R. Savinova, J. J. Gallet, F. Bournel, A. S. Gago and K. A. Friedrich, Highly Active Nano-Sized Iridium Catalysts: Synthesis and Operando Spectroscopy in a Proton Exchange Membrane Electrolyzer, *Chem. Sci.*, 2018, **9**, 3570–3579.

96 V. A. Saveleva, L. Wang, D. Teschner, T. Jones, A. S. Gago, K. A. Friedrich, S. Zafeiratos, R. Schlogl and E. R. Savinova, Operando Evidence for a Universal Oxygen Evolution Mechanism on Thermal and Electrochemical Iridium Oxides, *J. Phys. Chem. Lett.*, 2018, **9**, 3154–3160.

97 R. L. Doyle and M. E. G. Lyon, in *Photoelectrochemical Solar Fuel Production: From Basic Principles to Advanced Devices*, ed. S. Giménez and J. Bisquert, Springer International Publishing, Cham, 2016, pp. 41–104.

98 T. Shinagawa, A. T. Garcia-Esparza and K. Takanabe, Insight on Tafel Slopes from a Microkinetic Analysis of Aqueous Electrocatalysis for Energy Conversion, *Sci. Rep.*, 2015, **5**, 21.

99 D. Chandra, D. Takama, T. Masaki, T. Sato, N. Abe, T. Togashi, M. Kurihara, K. Saito, T. Yui and M. Yagi, Highly Efficient Electrocatalysis and Mechanistic Investigation of Intermediate $IrO_x(OH)_y$ Nanoparticle Films for Water Oxidation, *ACS Catal.*, 2016, **6**, 3946–3954.

100 J. O. Bockris, Kinetics of Activation Controlled Consecutive Electrochemical Reactions: Anodic Evolution of Oxygen, *J. Chem. Phys.*, 1956, **24**, 817–827.

101 Y. X. Zhao, N. M. Vargas-Barbosa, E. A. Hernandez-Pagan and T. E. Mallouk, Anodic Deposition of Colloidal Iridium Oxide Thin Films from Hexahydroxyiridate(IV) Solutions, *Small*, 2011, **7**, 2087–2093.

102 H. Dau, C. Limberg, T. Reier, M. Risch, S. Roggan and P. Strasser, The Mechanism of Water Oxidation: From Electrolysis via Homogeneous to Biological Catalysis, *ChemCatChem*, 2010, **2**, 724–761.

103 T. Reier, H. N. Nong, D. Teschner, R. Schlögl and P. Strasser, Electrocatalytic Oxygen Evolution Reaction in Acidic Environments – Reaction Mechanisms and Catalysts, *Adv. Energy Mater.*, 2017, **7**, 1601275.

104 S. Cherevko, Stability and Dissolution of Electrocatalysts: Building the Bridge between Model and "Real World" Systems, *Curr. Opin. Electrochem.*, 2018, **8**, 118–125.

105 K. J. J. Mayrhofer, D. Strmcnik, B. B. Blizanac, V. Stamenkovic, M. Arenz and N. M. Markovic, Measurement of Oxygen Reduction Activities Via the Rotating Disc Electrode Method: From Pt Model Surfaces to Carbon-Supported High Surface Area Catalysts, *Electrochim. Acta*, 2008, **53**, 3181–3188.